Plastic Stress Fields in the Region of Weld Toes for High-Strength Steels

M.Sc. Thesis

Subhi Abu Shetayyah

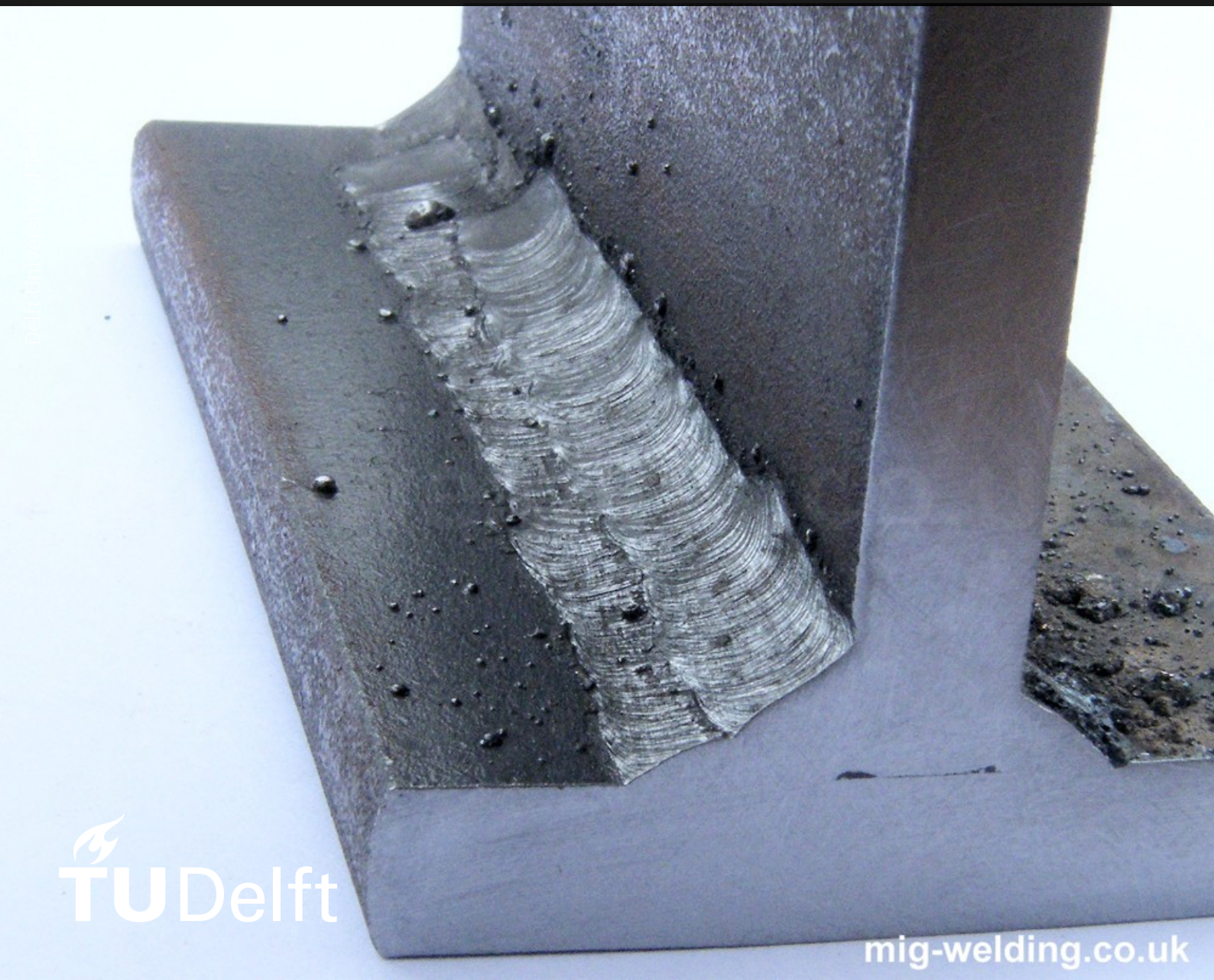

TU Delft

Plastic Stress Fields in the Region of Weld Toes for High-Strength Steels

M.Sc. Thesis

by

Subhi Abu Shetayyah

Student Name	Student Number
Subhi Abu Shetayyah	5842883

Instructor: C.Walters
Faculty: Faculty of Mechanical Engineering, Delft

TU Delft

Preface

Working on this thesis has been an intellectually stimulating and deeply rewarding journey. It has offered me the opportunity to delve into a challenging and meaningful topic that aligns closely with my professional aspirations. The exploration of high-strength steels and their application in structural engineering has not only enriched my knowledge but also reinforced my passion for solving complex engineering problems. I am grateful for every moment of discovery and learning that this process has brought.

I would like to express my heartfelt gratitude to my supervisor, Carey Walters, for his unwavering guidance, insightful feedback, and consistent support throughout the development of this work. His expertise and encouragement have been instrumental in shaping the direction and depth of my research. Beyond academic support, Carey Walters has helped me discover more about myself, particularly through the challenges and uncertainties I faced during this thesis.

This work would not have been possible without the love and encouragement of my family. To my parents and siblings, thank you for your constant belief in me, for the sacrifices you made, and for providing the foundation on which my ambitions are built. Your support has been the cornerstone of my achievements.

Finally, I want to acknowledge the many individuals whose efforts, directly or indirectly, have contributed to the completion of this thesis. Facing these challenges with the support of so many has not only shaped this thesis but has also helped me better understand myself and my capacity to overcome adversity.

This thesis represents the culmination of months of hard work and determination. It reflects not only my personal growth but also the invaluable contributions of the people who supported me throughout this journey. For this, I remain deeply thankful.

Subhi Abu Shetayyah
Delft, May 2025

Abstract

High-strength steels (HSS) are increasingly used in advanced engineering applications due to their exceptional mechanical properties. However, accurately predicting stress fields and localized yielding in welded joints—especially at sharp geometric features such as weld toes and notches—remains a significant challenge, particularly in the inelastic region. This thesis addresses this challenge by developing and validating an analytical framework based on the Strain Energy Density (SED) method for modeling localized structural behavior in HSS welded joints.

The foundational model extends a linear elastic formulation by den Besten to account for post-yield behavior. Three analytical approaches—Neuber's rule, Stowell's generalized approach, and Glinka's SED method—were critically assessed for the suitability of extending den Besten's equation, with Glinka's method selected for its ability to capture localized plasticity while maintaining computational efficiency. The model assumes localized plasticity surrounded by elastic behavior, and its predictions were verified against two bounding solutions: Irwin's ideal elastic–perfectly plastic lower bound and an extended linear elastic upper bound. Results consistently fell within these bounds, supporting the model's physical accuracy.

Numerical validation was also carried out using finite element analysis (FEA) in ANSYS on a Partially Penetrated Double-Sided (PPDS) T-joint configuration. Material modeling incorporated true stress–strain data, realistic weld geometry, and boundary conditions representative of actual welded joints. The simulation results showed strong agreement with the analytical predictions, particularly in the region of localized plasticity near the weld toe where the error was limited to up to about 3%.

This study confirms that the SED-based analytical method offers a practical and accurate approach for assessing welded joints with sharp notches—regions prone to stress singularities. The framework is computationally efficient, physically grounded, and broadly applicable across welded structures. Academically, it supports future research into refining boundary definitions, material models, and mesh optimization techniques. Practically, it enables safer and more efficient designs in HSS applications by providing engineers with reliable tools for evaluating post-yield structural behavior.

This thesis has been written entirely by the author. **ChatGPT** was utilized solely for refining the English language and enhancing readability. However, no AI-generated content has been incorporated into the research, technical analyses, methodology, or conclusions. All intellectual contributions, findings, and interpretations presented in this work are solely those of the author.

Contents

List of Figures

Nomenclature

Symbol	Description
A_n	Local notch area
C_{bm}	Membrane force-induced weld load carrying bending moments
C_{bb}	Bending moment-induced weld load carrying bending moments
E	Elastic modulus
E_s	Secant modulus
E'	Plane-strain-modified elastic modulus
FEA	Finite Element Analysis
FEM	Finite Element Method
HSS	High Strength Steels
H_k	Hollomon's strain hardening constant
K_t	Elastic stress concentration factor
K_{tx}	Modified elastic stress concentration factor
K'	Strength coefficient
L_P	Plastic limit load
L_w	Weld length or characteristic weld dimension
$PPDS$	Partially Penetrated Double-Sided
P	Parametric value describing weld geometry, $P = \log(t_c/2 + l_w)/t_b$
S	Nominal stress
S_{yx}	Modified yield initiation nominal stress
SCF	Stress Concentration Factor
W	Ratio of weld dimensions, h_w/l_w
e	Nominal strain
e_x	Modified nominal strain
r	Radial distance from weld toe
r_p	Plastic zone radius
t_b	Base plate thickness
t_p	Plate thickness
n'	Strain hardening exponent
α	Notch angle
β	Stress angle
μ or ν	Poisson's ratio
σ	Local notch stress
σ_b	Bending stress
σ_{bw}	Load carrying stress
σ_{eq}	Equivalent stress
σ_f	Far field stress
σ_m	Membrane stress
σ_n	Notch stress
σ_{nom}	Nominal stress
σ_{ref}	Thermal reference stress
σ_s	Structural stress
σ_{true}	True stress
$\sigma_{\theta\theta}$	Tangential stress
ϵ	Local notch strain
ϵ_{eq}	Equivalent strain
ϵ_{true}	True strain

1

Introduction

1.1. Problem Definition and Background

The use of high-strength steels (HSS), with yield strengths exceeding 550 MPa ($\sigma_y > 550$ MPa), has increased over the past two decades. This trend can be attributed to the rising financial considerations within the engineering industry and the market demands for stronger and larger structures. These demands necessitate the adoption of robust steels with reduced weight. In these applications, kilometers of welds are essential to the design, making the understanding and analysis of welds a crucial aspect of the construction process. Many of these large structures now utilize high-strength steels, underscoring the importance of comprehending the welding processes and characteristics specific to HSS. However, significant restrictions on the use of high-strength steels are imposed by design standards and codes, particularly for steels with high yield-to-tensile (Y/T) ratios [1]–[4]. Specifically, because when both the yield-to-tensile (Y/T) ratio and strain-hardening characteristics increase simultaneously, they raise the likelihood of the steel deviating from the desired ductile behavior typically exhibited by lower-strength steels.

Understanding the response of a structure when it undergoes local yielding is challenging, as it heavily depends on many different mechanical and geometrical properties, making it difficult to specify a general trend for the structure post yielding. Industry demands often focus on determining the highest tolerable Y/T ratio at which high-strength steels (HSS) can be utilized safely. This is in contrast to the limits set by design codes, which impose restrictions on the use of HSS due to their Y/T ratios [2]. These codes often limit the application of HSS based on potentially conservative Y/T ratio constraints. Consequently, the relationship between the strength of steels and their Y/T ratios, which goes hand in hand, complicates the unrestricted use of HSS without needing to comply with the design code limitations. Since these codes are designed to be as general as possible to account for a wide range of structural cases, they can be overly conservative in some scenarios. This highlights the importance of analyzing the post-yielding behavior of materials and structures, particularly for high-demand steels such as HSS. Therefore, outlining the following problem:

> *"How can the stress fields beyond the elastic limit be analyzed analytically while incorporating post yield hardening to describe the general behavior of high-strength steels with high Y/T ratios in the vicinity of a weld toe?"*

1.2. Problem Solution and Thesis Outline

To address this gap, this thesis develops an analytical formulation to describe the stress fields in question. The objective is to investigate the local structural response in the plastic region and characterize its behavior. The next chapter examines the current state of research on this topic, while subsequent chapters outline the methodology used to tackle the problem. Chapter 2, the Literature Review, provides a comprehensive overview of studies on high-strength steels (HSS), focusing on structural behavior in the inelastic region. Special attention is given to local structural response and assessment methods. The framework includes a detailed analysis of selected studies exploring the stress-strain behavior of

HSS structures beyond the elastic limit, particularly in welded joints. It also aims to define the characteristics of stress-strain fields and assess their implications for local integrity and structural design efficiency.

Building on the literature reviewed, the method to develop a general analytical expression to describe the plastic stress-strain field in high-strength steels (HSS) around weld toes becomes evident. While many existing studies focus on representing stress-strain fields in less generalized trends, this thesis aims to derive an analytical method that provides a more general and computationally friendly representation. Chapter 3 will detail the derivation of this method, incorporating and evaluating different approaches proposed in the literature to solve for stress-strain fields in elastic-plastic regions.

A numerical model, described in Chapter 4, will validate the analytical results and explore how different modeling setups can lead to variations in outcomes for the same case. This comparison will investigate the reasons behind potential differences between the models. Finally, the Conclusion (Chapter 5) will synthesize key insights gained from the results, comparing the outcomes of the analytical and numerical approaches and addressing possible sources of discrepancies.

1.3. Significance and Contribution

By optimizing the use of high-strength steel (HSS), significant financial benefits can be achieved—not only by reducing the amount of material required but also by minimizing welding material and labor, thereby decreasing the time needed to complete structures. Understanding the behavior of structures welded with high-strength steels, particularly in the post-yielding region, is essential for optimizing the use of these materials in various industries, such as the offshore and maritime industries. In steel structures, the most stressed regions are typically those surrounding welds; therefore, comprehending material behavior beyond yielding in these areas is critical for designers. When local yielding is anticipated, it is crucial to evaluate the structure's performance and determine whether additional reinforcement or load-transferring components are needed in those areas. Analyzing the local response beyond the yield limit, into the plastic region of the stress-strain curve, is fundamental for ensuring structural reliability and more optimized designs.

A key aspect of analyzing welded steel structures is the examination of stress and strain fields in highly localized regions. In welded joints, the area around the weld toe is particularly vulnerable to high stress concentrations due to design geometry and discontinuities introduced by the welding process. Academically, this study paves the way for further exploration into how different mechanical properties of HSS, as well as weld characteristics, influence structural behavior and performance. Notably, the proposed methodology is not limited to welds but can also be applied to other highly localized structures, such as notches or cracks. This approach eliminates the need for time-consuming experimental or numerical tests, providing an efficient analytical alternative for evaluating these critical regions.

2

Literature Review

2.1. Literature Overview

The use of steel structures has thrived for the past two centuries, with increasing demands for higher quality steel over time. In our current era, characterized by efficiency and economy, there is a heightened need for lightweight yet robust steel. This demand has led to the frequent adoption of high-strength steels, particularly in offshore applications [3]. Initially, high-strength steels saw limited application; for instance, in 2005, Eurocode 3 limited its scope to S460 [2]. However, in response to advancements in the industry, stronger steels like S960 are now being used [1]. This trend underscores the increasing and continuous relevance of high-strength steels till this day.

Understanding the stress and strain fields around welds is important, especially with the extensive use of welds in high-strength steels that have a high yield-to-tensile (Y/T) ratio, where material properties such as strain hardening become more critical. Discussions on the plastic distribution of stress and strains around welds, particularly at the weld toe, are often brief compared to other structural members in the literature. Even when welds are directly addressed, the focus is on how they act in the elastic region. However, the lack of comprehensive analytical research on stress-strain fields in the plastic region highlights the importance of exploring welded joints beyond the elastic limit. Existing papers that describe the plastic stress-strain fields around weld toes are often based on specific trends rather than general principles [5], [6].The models typically employed for analysis are often numerical or experimental. These approaches are generally not preferred due to their high costs in terms of time and effort, and their tendency to reflect on specific trends.

That is why initial efforts have focused on finding direct general analytical descriptions of plastic stress-strain fields for weld toes in high strength steels or steels with high Y/T ratios. Another relevant area of exploration is the analysis of notches, that is because they are also sensitive parts of the local structure often described in literature. Various papers have described the stress-strain fields around notches, specifically in the elastic-plastic region, making them fitting to this study [7]–[9]. Two methodologies that directly describe the stress-strain fields in the plastic region for notches will be discussed in this literature review to determine their applicability to welded joints, particularly weld toes. Although neither include the effect of HSS having a high Y/T ratio, the material properties could later be integrated in depth. The first and most common method is Neuber's method, in which Seeger and Heuler related nominal stresses and strains to local values and a generalized non-linear equation to determine actual stress and strain beyond the elastic limit for notches [8]. The second methodology is the strain energy density-based method, which assumes that plastic strain energy density can be calculated based on elastic stress-strain relations [7]. Both methodologies and their applicability to the issue at hand will be discussed further in the coming sections.

Another method mentioned in the literature, although it does not directly describe stress-strain fields beyond the proportionality limit, is an analytical model demonstrating the derivation of a plastic stress-strain field from an elastic one for a continuous plate with a circular hole [10]. Stowell, who had previously made the transition into the non-elastic region on a stress function, which is exactly what den

Besten and Kaminski had used for their description of the stress distribution for a welded joint in the elastic region [10], [11]. An analytical model proposing a descriptive elastic stress-strain field around a weld toe [11] could very possibly be used to analyze the welded joints beyond the elastic limit. This approach aims to transition the elastic stress-strain field around the weld toe to account for the inelastic region, potentially yielding a generalized trend for stress-strain fields around the weld toe within the plastic region of the stress-strain curve.

The following sections will provide detailed descriptions of selected literature and propose methodologies for further research in this thesis. A brief outline will demonstrate how the chosen literature will be utilized to address the research question posed, highlighting its relevance to the research topic in the next chapter.

2.2. Selected Literature

The literature search initially prioritized investigations into plastic stress-strain fields around weld toes. The method of literature review can be seen as a process of progressively broadening the scope over time, starting with a narrow focus and expanding to include more general studies on the topic. The following sections discuss the various methodologies and leads relevant to the topic at hand. Important questions such as the relevance and applicability of different methodologies to this literature review will be addressed.

2.2.1. The Generalized Neuber Method

As mentioned in the literature overview 2.1, Neuber's method is interesting because it is a commonly used approach for analyzing stress-strain fields beyond the elastic limit. This is primarily due to its accuracy in relation to computational cost. An article describing the generalized application of Neuber's method and how it can be correctly used to analyze notches in the net section with widespread plasticity is provided by Seeger and Heuler [8]. The well-known Neuber method equation is given by:

$$\sigma\epsilon = SeK_t^2 \tag{2.1}$$

The equation can be easily visualized by the following figure showing the area under the graph that is considered by Neuber and his law.

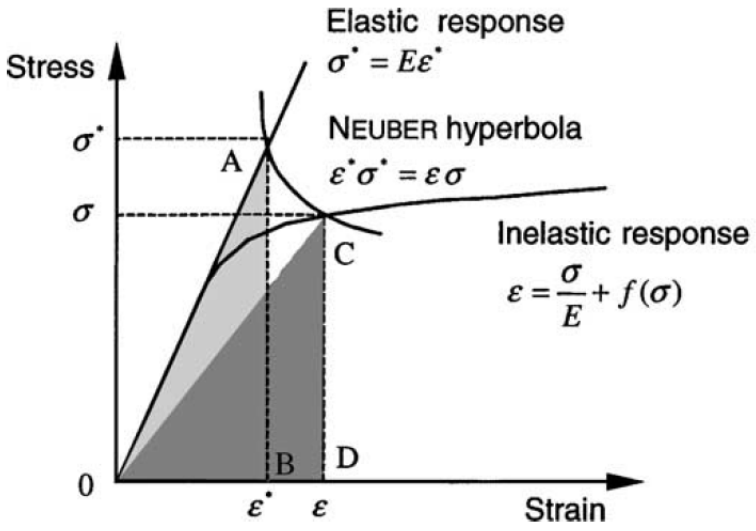

Figure 2.1: Illustration of Neuber's concept for estimating local stress-strain behavior using his equation, as described in [12].

Seeger and Heuler proposed a generalized equation that describes the fundamental mechanics based on simple formulations [8]. The authors believed that a generalized formulation of Neuber's method, which can be easily extended to accommodate specific cases, was the best solution. The generalized

Neuber equation suggested by Seeger and Heuler to account for the elastic-plastic region is given by:

$$\sigma\epsilon = K_t^2 \left(\frac{S^2}{E}\right)\left(\frac{Ee_x}{S_x}\right) \tag{2.2}$$

Where

- σ: Local notch stress.
- ϵ: Local notch strain.
- K_t: Elastic stress concentration factor, related to S.
- K_{tx}: Modified elastic stress concentration factor, related to S_x.
- E: Elastic modulus.
- e: Nominal strain.
- S: Nominal stress.
- e_x: Modified nominal strain.
- S_x: Modified nominal stress.
- S_{yx} Modified yield initiation nominal stress

The modified variables are to denote the incorporation of the inelastic behavior into the non-modified elastic variables. The significance of using the modified nominal stress, which incorporates σ_y (yield stress) and the fully plastic state of A_n (local notch area), arises when the material exceeds the yield limit. When dealing with an inelastic material, the simple linear relation cannot be used to identify the stress and strain since it no longer follows Hooke's law. The following equations are used to identify the nominal stress and the nominal strain, with g being a function of inelastic material behavior:

$$\sigma = g(\epsilon) \tag{2.3}$$

$$S = g(e) \tag{2.4}$$

The modified nominal stress that accounts for plasticity is a factor of $\frac{\sigma_y}{S_p}$ multiplied by the theoretical nominal stress:

$$S_x = S\left(\frac{\sigma_y}{S_p}\right) \tag{2.5}$$

Where σ_y is the yield stress and S_p refers to the nominal stress producing general yielding derived from L_p. L_p is defined as the plastic limit load for an elastic perfectly-plastic material law, and not the real ultimate load. L_p is calculated independently from the local stress-strain behavior from a uniaxial yield stress distribution in A_n, which is the area governing the fully plastic region with respect to equilibrium conditions. Note that it only accounts for uniaxial stresses and does not consider biaxial stresses, such as transverse stresses.

$$L_p = \sigma_y f(A_n) \tag{2.6}$$

However, as mentioned before, extra alterations using finite element analysis to account for multiaxial stresses are possible, which can provide L_p with good accuracy, even when Equation 2.6 cannot be used.

$$\sigma_e = SK_t = S_x K_{tx} \tag{2.7}$$

Here, the modified nominal stress and the stress concentration factor are related to calculate the theoretical elastic notch stress σ_e. The stress concentration factor K_t is calculated as follows:

$$S_{px} = \sigma_y \tag{2.8}$$

$$\sigma_y = S_{yx} K_{tx} \tag{2.9}$$

Rearranging the terms and dividing equations 2.8 & 2.9, the modified stress concentration factor that takes into account the plastic region is:

$$K_{tx} = \frac{S_{px}}{S_{yx}} \tag{2.10}$$

The stress-strain relation following Neuber's method can be written as:

$$\sigma\epsilon = S_x e_x (K_{tx})^2 \tag{2.11}$$

Finally, this leads to:

$$\sigma\epsilon = S^x K_{tx} e_x K_{tx} \frac{S_x E}{S_x E} \tag{2.12}$$

$$\sigma\epsilon = \frac{S^2 K_t^2}{E} \cdot \frac{e_x E}{S_x} \tag{2.13}$$

This provides the modified version of Neuber's formula to account for structural behavior post-yielding. The modified elastic stress concentration factor is assumed to be elastic. However, to account for the post-yielding material behavior, an additional factor is applied to address the yielding, in addition to the well-known Neuber's rule. If Hooke's law still applies, then $\frac{Ee^x}{S^x}$ is unity, which reduces to the well-known Neuber's equation.

2.2.2. The Strain Energy Density-Based Method

Glinka (1985) proposed an energy-based method to account for elastic-plastic stress-strain fields. Glinka assumed that the plastic energy could be described elastically. The validity of this assumption was discussed by comparing it to experimental test values [13]. The following assumptions were made by Glinka when applying the energy-based method: uniaxial loading was considered, and it was assumed that the material around the locally yielded region remained predominantly elastic. This assumption is reasonable since the majority of the strained material is elastic relative to the total energy strain. Therefore, the following relation can be applied for both the elastic region and the region where local yielding occurs:

$$K_t = \frac{\sigma}{S} \tag{2.14}$$

W_σ refers to the local strain energy per unit volume due to local stresses and W_S refers to the elastic energy strain due to the nominal stress S.

The stress concentration factor K_t with relation to the local energy stress and strains is:

$$K_t = \left(\frac{W_\sigma}{W_s}\right)^{0.5} \tag{2.15}$$

However, for the yielding region, a true stress-strain curve must be used to calculate the local strain energy. In this case, Glinka (1985) selected the well-known Ramberg-Osgood relation to account for the true stress-strain relationship [14]:

$$\epsilon = \frac{\sigma}{E} + \left(\frac{\sigma}{K'}\right)^{1/n'} \tag{2.16}$$

Which is then used in and substituted W_σ to account for local yielding to get the true stress. That follows :

$$W_\sigma = \frac{\sigma^2}{2E} + \frac{\sigma}{n'+1}\left(\frac{\sigma}{K'}\right)^{1/n'} \tag{2.17}$$

Substituting in the local energy strains into Equation 2.15 yields the final energy-based method relation to account for the elastic-plastic region:

$$K_t = \left\{ \frac{\frac{\sigma^2}{2E} + \left(\frac{\sigma}{K'}\right)^{1/n'} \frac{\sigma}{n'+1}}{\frac{S^2}{2E}} \right\}^{0.5} \tag{2.18}$$

Which can also be rewritten as:

$$\frac{(K_t S)^2}{2E} = \frac{\sigma^2}{2E} + \frac{\sigma}{n'+1}\left(\frac{\sigma}{K'}\right)^{1/n'} \tag{2.19}$$

In a study by Landgraf et al., the two methods for determining the elastic-plastic stress and strain fields in notched structures—the Neuber method and the energy-based method—were compared with calculated and measured results from various experiments [15]. The calculated results showed similar outcomes when the considered area on the stress-strain curve was within the elastic region; however, some discrepancies were observed between the different results.

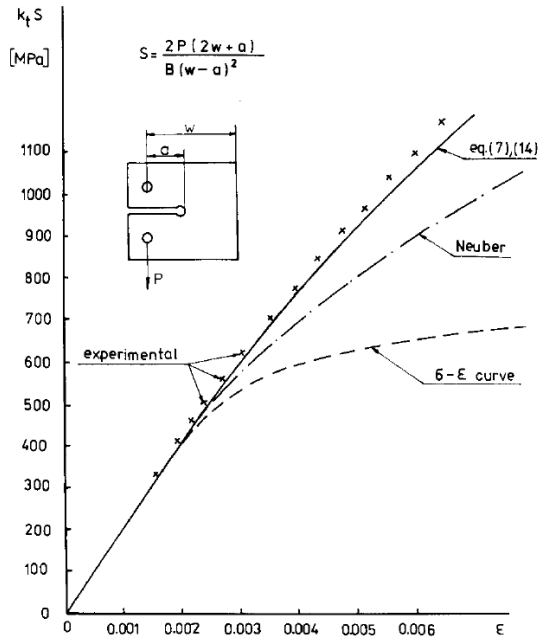

Figure 2.2: Comparison using a keyhole specimen to compare the accuracy of local strains between experimental and theoretical applications (Landgraf et al., 1975).

Glinka provided a brief introduction to the Neuber method and highlighted its differences from the energy-based method [7]. The main difference in results was that Neuber's method significantly overestimated the local plastic strains by approximately 30% compared to experimental results [7]. In contrast, the energy-based method showed a maximum of 2% difference between calculated and measured values. Furthermore, the energy-based method offered better accuracy without increasing computational effort compared to Neuber's method [15]. However, limitations exist when using the energy-based method. For this method to be applicable, the plastic yielding in the notch must be localized, with the plastic region being small compared to the surrounding elastic region. Additionally, the plastic zone depends on the nominal stress level, making the energy-based method applicable only when the nominal stress level is less than the yield limit. Figure 2.2 illustrates the difference in the results between experimental and calculated values.Up to the proportionality limit, the strain values showed minimal differences when compared to the experimental results. However, beyond this point, the accuracy of Neuber's results diminished relative to those within the elastic range. The energy-based method, as described in Equations 7 and 14, provided a good estimation of strain values even beyond the yield limit. Equations 7 and 14 referred to in the graph correspond to the following equations [2.16] & [2.19] respectively.

2.2.3. Stowell's Generalized Approach

A general transition method by Stowell [10] described the stress-strain field around a circular hole in a continuous plate, and then the transition of stress-strain fields from an elastic to an inelastic one using a function of the secant modulus. The secant modulus aids in characterizing the material's behavior, particularly within the nonlinear region. Figure 2.3 illustrates the secant modulus on a stress-strain curve, where the slope of the line connecting a chosen point in the inelastic region and the origin denotes the value of the secant modulus. Stowell used that concept to create a function that relates the secant modulus of the material in the vicinity of a hole to the secant modulus of the structure's material stress-strain curve [10].

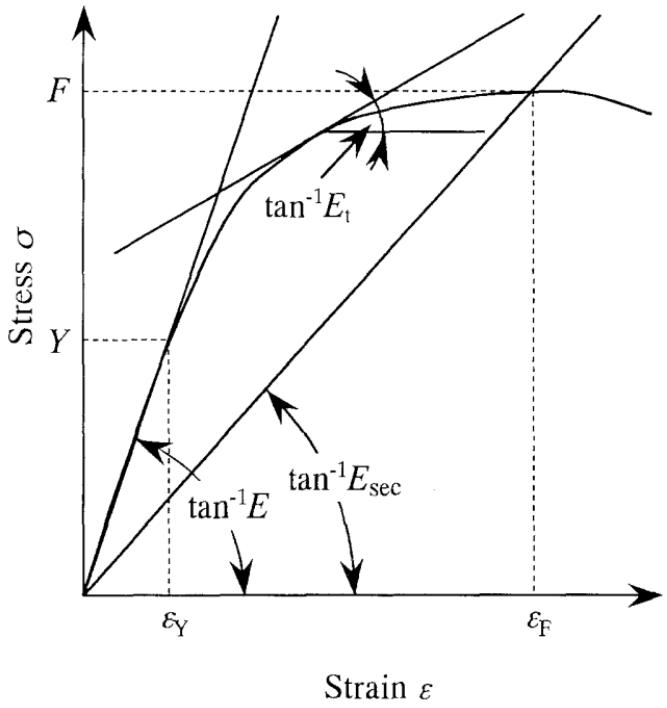

Figure 2.3: Graphical representation of the secant and tangent moduli on a stress–strain curve. The slope $\tan^{-1} E$ denotes the initial elastic modulus, $\tan^{-1} E_{\text{sec}}$ represents the secant modulus between the origin and a point on the curve, and $\tan^{-1} E_t$ indicates the tangent modulus at a specific strain level.

Stowell initially applied the stress and strain distribution around a circular hole as described by Kirsch [16], based on classical elasticity theory. This theory assumes the material obeys Hooke's law, expressed as $\sigma = E\epsilon$ [17]. The model considers an infinite plate with a circular hole of radius a, subjected to a uniform tensile stress σ_∞ applied, as illustrated in Figure 2.4.

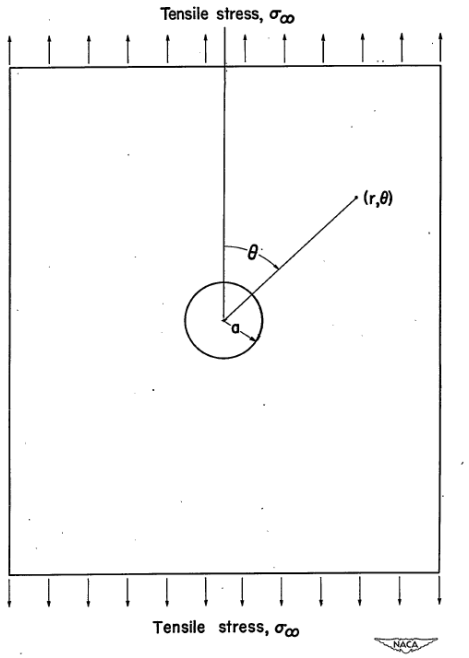

Figure 2.4: Idealized model of an infinite plate with a central hole of radius a, subjected to uniform tensile stress at infinity σ_∞, as used by Stowell (1950) for analytical calculations.

To calculate the Stress Concentration Factor (SCF) necessary for describing the stress distribution around the hole, the nominal stress must be related to the reference stress as follows: $K_t = \frac{\sigma}{S}$. In this case, the stress in the vicinity of a hole which represents the reference stress, σ, was calculated by summing up the normal tensile stress to the stress around a hole that was described by Kirsch [16]. Where the nominal stress, S, was just taken to be the longitudinal tensile stress at the ends of the plate. Stowell initiated the study by clarifying the phenomenon whereby the SCF of a continuous plate featuring a hole remains constant at 3 within the elastic threshold, a finding corroborated through experimental validation. However, by the definition of plasticity, it is expected for there to be a decrease in the stresses when entering the plastic region and an increase in the plastic strain when exceeding the elastic region due to the permanent deformation of the structure. The results of Stowell [10] were compared to what was given in his referenced study [18] which experimentally discussed the plastic flow of seven 24S-T4 Aluminum plates with a central circular hole. The experiments showed a decrease of the SCF for the Aluminum plates when exceeding the elastic limit from 3 to a 1.8 and for the plastic strain with an increase to 7.8 validating what Stowell had computed [18]. The analytical model proposed by Stowell relied on the utilization of the secant modulus, as defined as previously, to make a transition into the non elastic region. This transition facilitated the shift from the elastic field, previously established in a continuous plate with a circular hole, to the plastic domain.

In order to apply the Secant modulus effectively, it is important to adopt a general analytical approach to develop an expression capable of analyzing stresses and strains within the elastic region. A notable expression for such analysis was provided to evaluate the stress distribution across the width of a plate adjacent to a weld toe [11]. This analytical formulation describes the elastic stress-strain distribution field along the width of the base plate [11]. The geometrical symmetry of the weld could be both symmetrical or non-symmetrical with respect to half the plate thickness ($\frac{t_p}{2}$). Where the formulation distribution of the weld toe across the thickness of the base plate was computed analytically by considering the linear superposition of the far field stress $\sigma_f(\frac{r}{t_p})$, the weld load carrying stress $\sigma_{bw}(\frac{r}{t_p})$, and the tangential notch stress $\sigma_{\theta\theta}(\frac{r}{t_p})$ (refer to Figure 2.5).

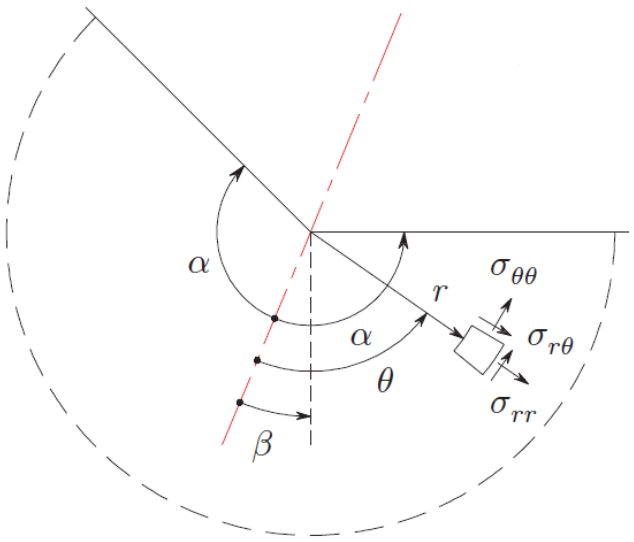

Figure 2.5: Stress contribution to a weld notch geometry based on the parameters defined by den Besten (2013).

Two of semi-analytical stress terms come due to the geometry of the welded joint, where the tangential stress can be clearly seen in the figure above. The weld load carrying stress can be described by the following formulation :

$$\sigma_s C_{bw} = \sigma_m C_{bm} + \sigma_b C_{bb} = \sigma_s \{C_{bm} - r_s(C_{bm} - C_{bb})\} \tag{2.20}$$

With

$$C_{bm} = \frac{m_{bm}\left(\frac{6}{t_p^2}\right)}{\sigma_{\sigma_s(1-r_s)}}$$

and

$$C_{bb} = \frac{m_{bb}\left(\frac{6}{t_p^2}\right)}{\sigma_{\sigma_s r_s}}$$

where

- σ_s: Structural stress.
- α: Notch angle.
- β: Stress angle.
- r_s: Structural bending stress ratio.
- m_{bb}: Bending moment induced weld load carrying bending moments.
- m_{bm}: Membrane force induced weld load carrying bending moments.
- σ_b: Bending stress.
- σ_m: Membrane stress.

and m_{bm} and m_{bb} are calculated using an FE beam model nodal forces. Where the final equation for the non-symmetrical case is then given as :

$$\begin{aligned}\sigma_n\left(\frac{r}{t_t p}\right) = \sigma_s \Bigg[&\Bigg[\left(\frac{r}{t_p}\right)^{\lambda_s - 1} \mu_s \lambda_s(\lambda_s+1)\cos(\lambda_s+1)\beta - \chi_s \cos(\lambda_s - 1)\beta\Bigg] \\ &+ \left[\left(\frac{r}{t_p}\right)^{\lambda_a - 1} \mu_a \lambda_a(\lambda_a+1)\cos(\lambda_a+1)\beta - \chi_a \cos(\lambda_a - 1)\beta\right] \\ &+ C_{bw}\left[2\left(\frac{r}{t_p}\right) - 1\right] - 2r_s\left(\frac{r}{t_p}\right)\Bigg]\end{aligned} \tag{2.21}$$

2.3. Discussion

This chapter provides a comprehensive exploration of the research and methodologies associated with analyzing plastic stress and strain fields, particularly for high-strength steels and welded joints. The increasing demand for high-strength steels, driven by financial considerations and the need for lightweight yet robust materials in engineering applications, underscores the importance of understanding the behavior of these materials under various loading conditions, especially in welds around weld toes. The review highlights the need for describing a general trend for the plastic stress-strain field around weld toes.

In this chapter, various methodologies have been explored for analyzing plastic stress-strain fields around local weld toe configurations, focusing primarily on the Neuber method and the SED (Strain Energy Density) also known as the energy-based method. Additionally, the idea of trying to integrate various methods to come up with a general analytical trend for plastic stress-strain fields was studied, which involves transitioning from elastic to inelastic stress-strain fields utilizing Stowell's generalized approach. Neuber's method, as discussed, is a widely used approach for analyzing stress-strain fields beyond the elastic limit due to its balance between accuracy and computational cost. However, its primary drawback lies in its tendency to overestimate local plastic strains. This overestimation, as observed by Landgraf et al., can be as high as 30% compared to experimental results [15]. The fundamental Neuber equation $\sigma\epsilon = SeK_t^2$ provides a straightforward calculation for the elastic region but fails to accurately account for the complexities of the elastic-plastic transition. In contrast, the energy-based method proposed by Glinka (1985) offers a more accurate representation of the elastic-plastic stress-strain fields [14]. By assuming that the plastic strain energy density can be approximated fully elastically, this method ensures that the local strain energy is a true reflection of the material's behavior at the notch root. The energy-based method demonstrated only a 2% difference between calculated and measured values, significantly outperforming the Neuber method in terms of accuracy without increasing computational effort. The integration of the Ramberg-Osgood relation into this method allows for a precise calculation of the true stress-strain relationship in the yielding region.

While the energy-based method offers advantages over the generalized Neuber method, it has limitations in accurately predicting stresses and strains in plane stress conditions. Glinka (1985) observed that the generalized Neuber method performs best for thin-walled structures or those under plane stress, but its accuracy significantly diminishes in plane strain scenarios [14]. Another key limitation is the assumption that the plastic region is sufficiently small so that the total strain energy can be considered as confined within the elastic region. In this study, the integrated method was applied to the elastic stress–strain field described by den Besten (2013), which uses a stress function approach similar to that developed by Stowell [10]. Stowell investigated steel sheets under tension with a central hole—a scenario producing localized plasticity—which makes it relevant to explore how well a similar plastic transition method could be incorporated into den Besten's analytically defined stress–strain distribution [11].

In summary, this literature review lays the groundwork for further research into calculating and characterizing stress and strain fields in high-strength steels and welded joints. The literature highlights the importance of discussing how a welded joint behaves with high-strength steel after yielding, making use of an analytical model. Although current literature provides some solutions, it does not specifically describe how a welded joint with high-strength steels and strain hardening effects behaves post-yielding. This is a crucial point for designers to try and optimize their designs by analyzing fracture limits and their potential occurrence. Which is why the same question persists:

> *"How can a general analytical expression be developed to describe stress fields in high-strength steels with post-yielding strain hardening in the vicinity of weld toes?"*

This subsequent chapters provide the framework required to address the central question at hand.

3

Analytical Model

3.1. Analytical Model Outline

This chapter provides a detailed description of the analytical model developed to solve for the post-yielding material behavior in the region around a weld toe based on the suggested methods discussed in the previous chapter. It also explains the rationale behind the chosen parameters, highlights the utility of the analytical model, and outlines the results and how they will be verified. The analytically derived method is intended to be broadly applicable, with the specific adaptation for including the inelastic stress field near a weld toe achieved by modifying a general elastic analytical expression to account for inelastic behavior.

This study focuses on welded structures, specifically a partially penetrated double-sided (PPDS) welded T-joint. Particular emphasis is placed on the weld toe, a critical region for designers, as it is the first area likely to yield, especially under Mode-I type loading. Understanding both the yielding and post-yielding phases around the weld toe is therefore considered the aim of the research.

In addition to the general analytical model to be developed, which aims to accurately represent the structural behavior beyond the yield limit, two other stress fields will be presented as boundary cases: one assuming fully elastic behavior even post yielding and the other assuming elastic-perfectly-plastic behavior. These cases provide upper and lower bounds, respectively, establishing a range for the results. The following sections of this chapter provide a more detailed explanation of these concepts and the parameters used to describe the stress fields around weld toes. The three results will then be compared to initially evaluate the effectiveness of the analytical method employed. These results will subsequently be validated against the numerical method in later chapters to confirm the accuracy and reliability of the analytical approach outlined in this chapter.

3.2. The Analytical Framework

3.2.1. Linear Elastic Stress Field Around a Weld Toe

The three analytical methods extracted from the literature were evaluated by the author to adjust a purely elastic stress field to one that incorporates inelastic behavior. Each method starts with a linear elastic stress–strain field, which is then extended to account for material yielding and post-yield effects. In this study, the linear elastic formulation developed by den Besten [11]—which describes the stress distribution near a weld toe as a function of the base plate thickness—was selected as the foundational elastic expression. This formulation was integrated into each method to assess its effectiveness in capturing the transition from elastic to inelastic behavior. The fundamental elastic equation is given by

[11]:

$$\begin{aligned}\sigma_n\left(\frac{r}{t_p}\right) = \sigma_s \Bigg[&[\left(\frac{r}{t_p}\right)^{\lambda_s - 1} \mu_s \lambda_s (\lambda_s + 1)\cos{(\lambda_s + 1)\beta} - \chi_s \cos{(\lambda_s - 1)\beta}\Bigg] \\ &+ \left[\left(\frac{r}{t_p}\right)^{\lambda_a - 1} \mu_a \lambda_a (\lambda_a + 1)\cos{(\lambda_a + 1)\beta} - \chi_a \cos{(\lambda_a - 1)\beta}\right] \\ &+ C_{bw}\left[2\left(\frac{r}{t_p}\right) - 1\right] - 2r_s\left(\frac{r}{t_p}\right)]\end{aligned} \tag{3.1}$$

A similar equation, also proposed by den Besten, describes the stress distribution at the weld root [11]. This equation can also be adapted and transitioned in the same manner as the primary equation mentioned above to account for yielding, as detailed in the following sections. However, the modifications to the equation based on the weld root will not be addressed or described in detail in this study.

Equation 3.1 considers the linear superposition of the following three contributions:

- The far-field stress - σ_f
- The weld load-carrying stress - σ_{bw}
- The geometry notch-related stresses - $\sigma_{\theta\theta}$

The T-joint, shown in Figure 3.1, was selected for analysis due to its widespread use as one of the most common weld types. This configuration is particularly relevant for studying notches and the surrounding material, which are critical concerns for structural engineers. These areas become especially important in the post-yield phase, where accounting for the material's nonlinear behavior adds significant complexity to the overall structural response.

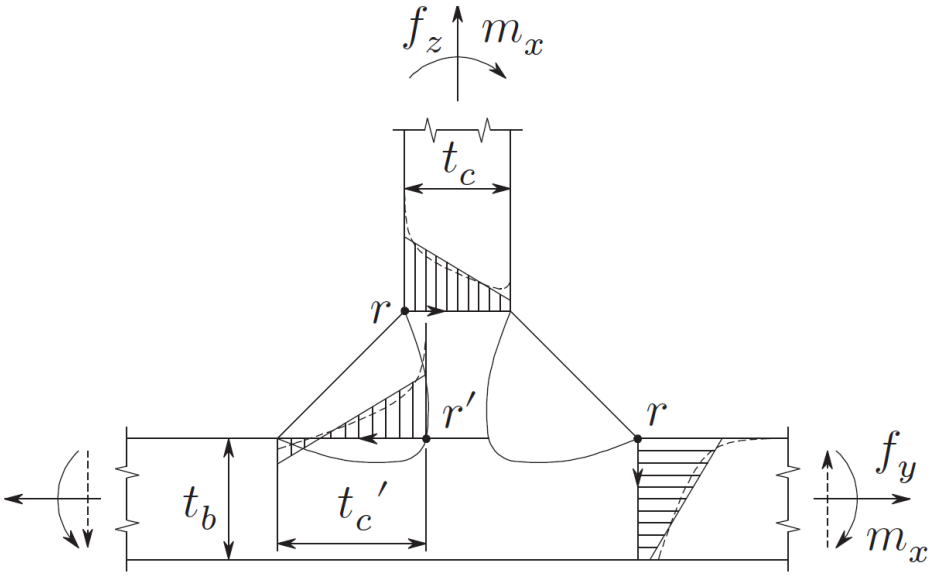

Figure 3.1: PP DS T-joint with Mode-I type loading [11]

The classification of welds is primarily based on four key factors:

- Weld type (groove or fillet)
- Geometrical Properties
- The HS (hotspot) classification
- The loading mode

The weld classifications outlined above are crucial for predicting the types of stresses that may arise and identifying which part of the joint is most likely to yield first. This understanding is vital for accurately

analyzing post-welding behavior. In the case under study, T-joints are fillet welds with a non-symmetric geometry relative to $\frac{t_b}{2}$, the base plate thickness, as shown in Figure 3.1. Based on the classifications above and considering Mode I loading, the joint is categorized as an HS (hotspot) type C, where stress is distributed along the seam. Consequently, the primary stresses anticipated are those acting along the thickness of the base plate, referred to as t_b in Figure 3.1.

For this reason, the analytical Equation 3.1, which captures the stresses through the thickness of the base plate, will serve as the foundation for testing the stress fields in this study. It is important to note that the four weld classifications under consideration will remain constant throughout the analysis. This consistency ensures that the comparison and evaluation of stress-strain fields are carried out within the same classification framework, allowing for reliable and accurate comparisons in the following chapters.

The three stress contributions used in equation 3.1 far-field stress (σ_f), notch geometry related stress ($\sigma_{\theta\theta}$), and weld-load carrying stress (σ_{bw}) can be calculated individually to determine their respective contributions. These components are described as follows:

Far Field Stress

$$\sigma_f\left(\frac{r}{t_p}\right) = \sigma_s\left\{1 - 2r_s\left(\frac{r}{t_p}\right)\right\} \quad \forall\left\{0 \leq \left(\frac{r}{t_p}\right) \leq 1\right\} \tag{3.2}$$

Where σ_s represents the structural stress, r_s denotes the structural bending stress ratio, and the $\frac{r}{t_p}$ ratio specifies the location being tested across the thickness of the base plate. The ratio $\frac{r}{t_p} = 0$ corresponds to r being at the closest point to the weld toe (location zero relative to the base plate), while $\frac{r}{t_p} = 1$ indicates $r = t_p$, which corresponds to the full thickness of the base plate or the point furthest from the weld toe, i.e., the bottom of the base plate.

Weld Load Carrying Stress

The weld load-carrying stress (σ_{bw}) refers to the stress carried by the weld when the neutral axis shifts due to the weld geometry.

$$\sigma_{bw}\left(\frac{r}{t_p}\right) = \sigma_s C_{bw}\left[\left\{4\left(\frac{r}{t_p}\right) - 1\right\} + 6\left(\left(\left(\frac{r}{t_p}\right) - \frac{1}{2}\right)^2 - \frac{1}{12}\right)\right] \tag{3.3}$$

$\sigma_s C_{bw}$ is given by:

$$\sigma_s C_{bw} = \sigma_m C_{bm} + \sigma_b C_{bb} = \sigma_s\left\{C_{bm} - r_s(C_{bm} - C_{bb})\right\} \tag{3.4}$$

where,

$$C_{bm} = \frac{m_{bm}\left(\frac{6}{t_p}\cdot\frac{2}{2}\right)}{\sigma_s(1 - r_s)}, \quad C_{bb} = \frac{m_{bb}\left(\frac{6}{t_p}\cdot\frac{2}{2}\right)}{\sigma_s r_s} \tag{3.5}$$

The m_{bm} and m_{bb} terms, represent the membrane bending moment and the bending moment, respectively, are estimated through Finite Element (FE) analysis, as described by den Besten in equation 3.1 [11]. However, this estimation is not applicable to all geometries in general cases. To address this limitation, Qin et al., utilized parametric equations to account for and calculate these terms, enabling a more general trend for the weld load-carrying stress component of the equation [28]. The parametric equations are given as:

$$C_{bm} = 0.117 - 0.192\cdot e^{-0.494\cdot W} + \frac{0.793\cdot P^3 + 1.113\cdot P^2 + 0.957\cdot P + 0.9}{P^4 + 4.721\cdot P^3 + 13\cdot P^2 + 9.669\cdot P + 9.079}. \tag{3.6}$$

$$C_{bb} = 0.123 - 0.261\cdot e^{-0.712\cdot W} + \frac{0.143\cdot P^4 + 1.007\cdot P^3 + 1.438\cdot P^2 + 1.674\cdot P + 1.578}{P^4 + 3.892\cdot P^3 + 9.41\cdot P^2 + 7.57\cdot P + 8.118}. \tag{3.7}$$

$$W = \left(\frac{h_w}{l_w}\right). \tag{3.8}$$

$$P = \log\left(\frac{t_c/2 + l_w}{t_b}\right). \tag{3.9}$$

Notch Geometry Related Stress

Finally, the notch geometry-related stress is expressed as:

$$\begin{aligned}\sigma_{\theta\theta}\left(\frac{r}{t_p}\right) = \sigma_s \left(\frac{r}{t_p}\right)^{\lambda_s-1} &\left[\mu_s\lambda_s(\lambda_s+1)\cos\big((\lambda_s+1)\beta\big) - \chi_s\cos\big((\lambda_s-1)\beta\big)\right] \\ + \left(\frac{r}{t_p}\right)^{\lambda_a-1} &\left[\mu_a\lambda_a(\lambda_a+1)\sin\big((\lambda_a+1)\beta\big) - \chi_a\sin\big((\lambda_a-1)\beta\big)\right].\end{aligned} \tag{3.10}$$

The parameters μ_s and μ_a represent the stress amplitude of the symmetric and anti-symmetric components, respectively, and are given by:

$$\begin{aligned}\mu_s &= \frac{C_{bw}(\lambda_a+1)+3(\lambda_a-1)}{6(\lambda_a-\lambda_s)\left[\cos\big((\lambda_s+1)\beta\big) - \chi_s\cos\big((\lambda_s-1)\beta\big)\right]} \\ \mu_a &= \frac{-C_{bw}(\lambda_a+1)-3(\lambda_a-1)}{6(\lambda_a-\lambda_s)\left[\sin\big((\lambda_a+1)\beta\big) - \chi_a\sin\big((\lambda_a-1)\beta\big)\right]}.\end{aligned} \tag{3.11}$$

Here, β and α denote the stress and notch angles, respectively.

$$\begin{aligned}\alpha &= \frac{1}{2}\left\{\pi + \arctan\left(\frac{h_w}{l_w}\right)\right\} \\ \beta &= \alpha - \frac{\pi}{2}\end{aligned} \tag{3.12}$$

Linearly summing the three stress contributions yields equation 3.1, which is originally defined for elastic stress fields.

The equation describing the notch stress along the plate thickness is particularly valuable because it captures both plane stress and plane strain responses. This is achieved through a modern approach using the Airy stress function, as implemented by den Besten [11]. The method simplifies the analysis by expressing all boundary conditions consistently—either entirely in terms of forces and moments or entirely in terms of displacements—allowing for a unified treatment of different structural states.

3.2.2. Different Transition Methodologies

As discussed in the literature review, the various transition methodologies from accounting for elastic to elastic-plastic fields will be compared. The primary transition methodologies to be examined are as follows:

- Generalized Stowell's method
- Neuber's method
- The SED (strain energy density) method as described by Glinka

3.2.3. Generalized Stowell's Method

The incorporation of the secant modulus, as introduced by Stowell, was implemented by applying a function of the secant modulus to an elastic model. Stowell demonstrated this approach for the stress-strain field described by Kirsch [16] in the case of a circular hole under uniaxial tension in an infinitely long plate [10]. In this approach, the function of the secant modulus was applied to the analytical expression for elastic stress components that explicitly presented elastic material properties, effectively enabling the inclusion of yielding material behavior.

A similar adaptation was intended for equation 3.1, but it could not be directly applied. This limitation arises because the material properties in equation 3.1 are implicitly embedded within the equation itself. Den Besten employs a scalar stress function (Airy stress function) and Williams' equation to address the singularity at a notch radius of $\rho = 0$ in polar coordinates [11]. The resulting formulation is expressed as follows:

$$\varphi = r^{\lambda+1}\cdot\left[C_1\cos\big((\lambda+1)\theta\big) + C_2\cos\big((\lambda-1)\theta\big) + C_3\sin\big((\lambda+1)\theta\big) + C_4\sin\big((\lambda-1)\theta\big)\right] \tag{3.13}$$

The governing equation for the Airy stress function in elasticity problems is the biharmonic equation. By using this representation, determining stresses in an elastic body is reduced to solving (3.21), provided that the derivatives meet the appropriate boundary conditions.

The Laplacian of a scalar function φ in polar coordinates is given by:

$$\nabla^2\varphi = \frac{\partial^2\varphi}{\partial r^2} + \frac{1}{r}\frac{\partial\varphi}{\partial r} + \frac{1}{r^2}\frac{\partial^2\varphi}{\partial\theta^2}. \tag{3.14}$$

The biharmonic equation arises in the theory of elasticity. The derivation starts from the compatibility condition for plane strain:

$$\frac{\partial^2\sigma_{xx}}{\partial y^2} - \nu\frac{\partial^2\sigma_{yy}}{\partial y^2} - 2(1+\nu)\frac{\partial^2\sigma_{xy}}{\partial x\partial y} + \frac{\partial^2\sigma_{yy}}{\partial x^2} - \nu\frac{\partial^2\sigma_{xx}}{\partial x^2} = 0, \tag{3.15}$$

where ν is Poisson's ratio.

The stress components can be expressed in terms of the Airy stress function $\phi(x, y)$ as:

$$\sigma_{xx} = \frac{\partial^2\phi}{\partial y^2}, \quad \sigma_{yy} = \frac{\partial^2\phi}{\partial x^2}, \quad \sigma_{xy} = -\frac{\partial^2\phi}{\partial x\partial y}. \tag{3.16}$$

Substituting (3.16) into (3.15) yields:

$$\begin{aligned}&\frac{\partial^2}{\partial y^2}\left(\frac{\partial^2\phi}{\partial y^2}\right) - \nu\frac{\partial^2}{\partial y^2}\left(\frac{\partial^2\phi}{\partial x^2}\right)\\ &- 2(1+\nu)\frac{\partial^2}{\partial x\partial y}\left(-\frac{\partial^2\phi}{\partial x\partial y}\right) + \frac{\partial^2}{\partial x^2}\left(\frac{\partial^2\phi}{\partial x^2}\right) - \nu\frac{\partial^2}{\partial x^2}\left(\frac{\partial^2\phi}{\partial y^2}\right) = 0.\end{aligned} \tag{3.17}$$

Simplifying the derivatives:

$$\frac{\partial^4\phi}{\partial y^4} - \nu\frac{\partial^4\phi}{\partial x^2\partial y^2} + 2(1+\nu)\frac{\partial^4\phi}{\partial x^2\partial y^2} + \frac{\partial^4\phi}{\partial x^4} - \nu\frac{\partial^4\phi}{\partial x^2\partial y^2} = 0. \tag{3.18}$$

Combine like terms in (3.18):

$$\frac{\partial^4\phi}{\partial x^4} + \underbrace{[-\nu + 2(1+\nu) - \nu]}_{=2}\frac{\partial^4\phi}{\partial x^2\partial y^2} + \frac{\partial^4\phi}{\partial y^4} = 0. \tag{3.19}$$

This reduces to:

$$\frac{\partial^4\phi}{\partial x^4} + 2\frac{\partial^4\phi}{\partial x^2\partial y^2} + \frac{\partial^4\phi}{\partial y^4} = 0, \tag{3.20}$$

which is equivalent to the biharmonic operator in Cartesian coordinates:

$$\left(\frac{\partial^2}{\partial x^2} + \frac{\partial^2}{\partial y^2}\right)^2\phi = \nabla^4\phi = 0. \tag{3.21}$$

As shown in the derivation of the biharmonic equation, the material properties are implicitly embedded within the formulation through the constitutive relations. This complexity necessitates the development of an entirely new equation that goes beyond purely elastic material behavior to include post-yield inelastic components. Instead of adapting the existing linear elastic formulation presented in Equation 3.1, this new approach requires deriving the governing equations directly from equilibrium and compatibility conditions, thereby incorporating plastic strains from the outset.

In contrast, Stowell's method takes a more direct route by explicitly embedding material-related terms into the linear fundamental equation, simplifying the analysis. He introduced a secant modulus function, derived and integrated into the stress–strain field equation for circular geometries. By embedding the secant modulus into the formulation at points where material properties are explicitly defined, the method extends the analysis to capture both elastic and inelastic behavior within a linearized analytical framework. However, this approach diverges from the original intent of preserving the analytical structure established by den Besten [11], which sought a more seamless transition from elastic to inelastic behavior.

Strain Energy Density and the Neuber's Method

In this section, the other two methods will be discussed together due to certain similarities within the elastic region and other comparisons that call for evaluation. These comparisons will ultimately highlight why the SED method is chosen over Neuber's method to describe the stress-strain fields around a weld toe for plane strain conditions.

The SED method, as introduced by Glinka, emphasizes how a notch effects cause significant variations in stress-strain energies across different regions of the local structure [14]. This observation motivated the consideration of stress-strain fields in terms of energy strain densities. To describe stresses and strains in terms of energy densities, the following relations are derived to calculate the strain energy density per unit volume due to local stresses and strains, as well as the elastic strain energy density per unit volume due to nominal stresses, respectively:

$$W_\sigma = \int_0^\epsilon \sigma(\epsilon)\, d\epsilon = \int_0^\epsilon E\epsilon\, d\epsilon = E\frac{\epsilon^2}{2} = \frac{\sigma^2}{2E} \tag{3.22}$$

$$W_s = \int_0^e S(e)\, de = \int_0^e Ee\, de = E\frac{e^2}{2} = \frac{S^2}{2E} \tag{3.23}$$

The similarities mentioned earlier between Neuber's Method and the SED method in the elastic region can be observed in the following relation, which relates the theoretical stress concentration factor, K_t, to the strain energy:

$$K_t = \frac{\sigma}{S} \tag{3.24}$$

This relation can further be expressed as:

$$K_t = \left(\frac{W_\sigma}{W_s}\right)^{0.5} \tag{3.25}$$

Graphical representations of these relationships in the elastic and elastic-plastic ranges given by Glinka are shown below:

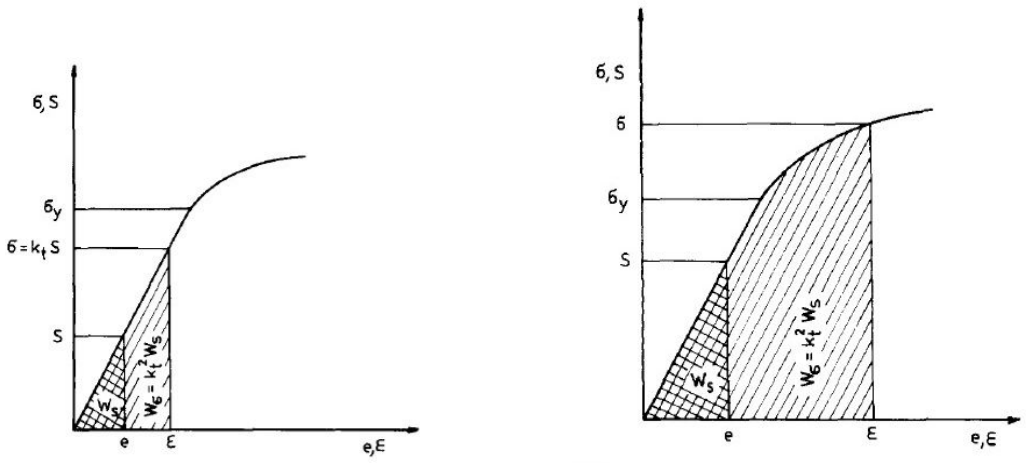

(a) Elastic region representation. **(b)** Inelastic region with energy distribution.

Figure 3.2: Stress-strain diagrams illustrating the calculation of strain energy density (SED) areas before and after yielding, based on the method by Glinka [14].

As illustrated in the stress-strain curve above, the strain energy density for any part of the elastic region can be calculated with ease and is consistent with every method. However, challenges arise when

attempting to account for the inelastic region, where discrepancies between different methods become evident. Glinka, in addressing the effects of notches, proposed a reasonable assumption: the strain energy density of a very localized area of the structure can be equated to the strain energy density of the surrounding governing area. This assumption considers that the localized inelastic behavior is governed by the elastic behavior of the larger bounded area around it as shown numerically below in Equation 3.26.

$$W_S = W_\sigma \quad \text{or} \quad \int_0^{e_{ij}} S_{ij}\, d\epsilon_{ij} = \int_0^{\epsilon_{ij}} \sigma_{ij}\, d\epsilon_{ij}. \tag{3.26}$$

In this context, as a localized stress-strain field is being analyzed and the area around the notch is predominantly governed by linear elastic behavior, Glinka introduced an assumption for cases involving localized plastic yielding. Specifically, the plastic strain energy density in the plastic region of the stress-strain field is assumed to be equal to, or approximately the same as, the strain energy density of the linear elastic material in the surrounding region of the structure. This localized assumption implies that the theoretical stress relation also holds in Equation 3.25, but with the material property modified to account for inelastic behavior. To achieve this, Glinka [14] employed the well-known material property described by the Ramberg-Osgood equation:

$$\epsilon = \frac{\sigma}{E} + \left(\frac{\sigma}{K}\right)^{1/n} \tag{3.27}$$

To apply the Ramberg-Osgood equation, as presented in Equation (3.27), to the strain energy density W_σ, a mathematical manipulation of the integral is performed. The integrand of the equation can then be rewritten as follows:

$$\sigma d\epsilon = \epsilon d\sigma + \sigma d\epsilon - \epsilon d\sigma. \tag{3.28}$$

This formulation leads to the complete expression for the strain energy density W_σ:

$$W_\sigma = \int [d(\sigma\epsilon) - \epsilon d\sigma] = \sigma\epsilon - \int_0^\sigma \epsilon d\sigma. \tag{3.29}$$

Substituting the material model from Equation (3.27) into the modified formulation of the strain energy density given in Equation (3.29), we obtain:

$$W_\sigma = \int_0^\epsilon \sigma(\epsilon)\, d\epsilon = \frac{\sigma^2}{2E} + \frac{\sigma}{n'+1}\left(\frac{\sigma}{K'}\right)^{1/n'}. \tag{3.30}$$

To incorporate Glinka's assumption of general elastic yielding [14] and apply her method, the following expression is derived:

$$\left(\frac{W_\sigma}{W_s}\right)^{0.5} = k_t = \left\{\frac{\frac{\sigma^2}{2E} + \frac{\sigma}{K'}^{1/n'}\sigma/(n'+1)}{S^2/2E}\right\}^{0.5}. \tag{3.31}$$

Rearranging and simplifying, we obtain:

$$\frac{(k_t S)^2}{2E} = \frac{\sigma^2}{2E} + \frac{\sigma}{n'+1}\left(\frac{\sigma}{K'}\right)^{1/n'}. \tag{3.32}$$

Assuming that the nominal stress exceeds the yield stress of the material, the equation takes the following form:

$$K_t^2\left[\frac{S_n^2}{2E'} + \frac{S_n}{n+1}\left(\frac{S_n}{K'}\right)^{1/n'}\right] = \frac{(\sigma_y')^2}{2E'} + \frac{\sigma_y'}{n'+1}\left(\frac{\sigma_y'}{K'}\right)^{1/n}. \tag{3.33}$$

In this case, the stress concentration factor K_t is assumed to be the theoretical elastic stress concentration factor, derived from the full elastic solution in Equation (3.1). This assumption considers K_t as the ratio of the reference stress to the structural stress at every point along the base plate thickness.

Similarly, the nominal stress S_n varies the same way across the thickness of the base plate, following a ratio of $\frac{r}{t_b}$, where a value of zero corresponds to the region closest to the notch, and a value of one represents the region farthest away.

Here, apostrophes denote plane strain conditions, recognizing that material properties may differ between plane stress and plane strain states. The corresponding strain equation is given by:

$$\epsilon'_y = \frac{\sigma'_y}{E'} + \left(\frac{\sigma'_y}{K'}\right)^{1/n'}. \tag{3.34}$$

- ϵ'_y: Strain at yield, accounting for plane strain conditions.
- σ'_y: Local Stress, accounting for plane strain conditions.
- E': Young's modulus, accounting for plane strain conditions.
- K': Strength coefficient, accounting for plane strain conditions.
- n': Strain hardening exponent, accounting for plane strain conditions.

3.2.4. Distinguishing Features of Energy Based Approach and Neuber Approach

The Strain Energy Density (SED) method was explained in the previous section, and not much difference can be observed between the energy-based approach and Neuber's method in the elastic region. In fact, within the linear elastic region, the equations are identical. However, significant differences emerge when the inelastic region of the material is considered. This divergence arises because Neuber simplifies the inelastic behavior of the material. Neuber's expression is given as:

$$\sigma\epsilon = SeK_t^2 \tag{3.35}$$

This formulation implies that no integration is performed over the area under the inelastic portion of the stress–strain curve. Instead, a constant value is assumed, and the inelastic region is represented as the product of the stress concentration factor and the elastic stresses and strains. A graphical representation by Glinka effectively illustrates the key differences between these two approaches:

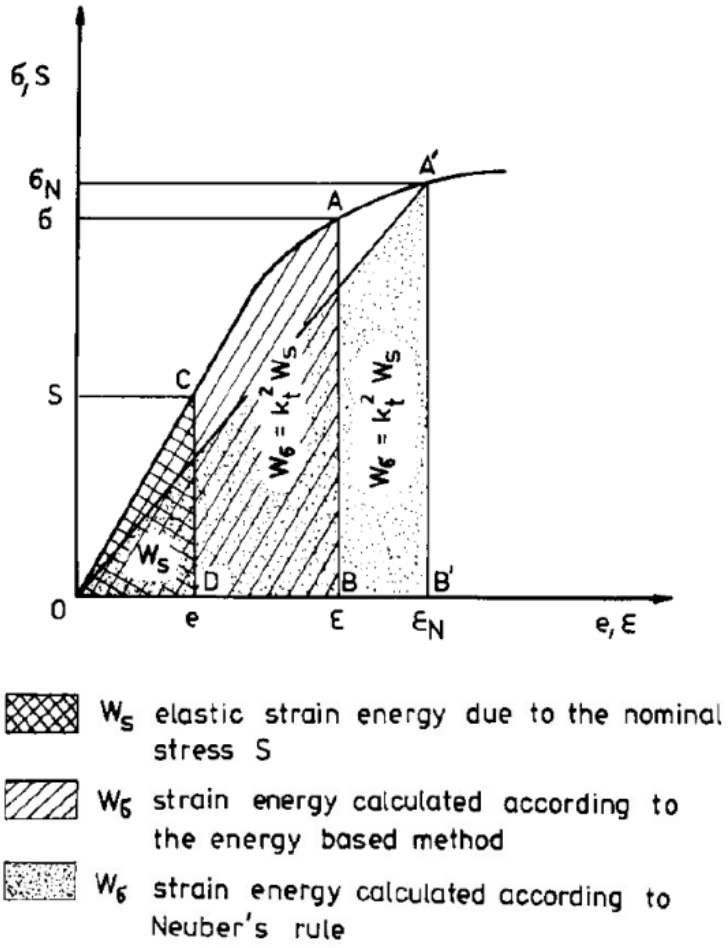

Figure 3.3: Graphical representation clarifying the differences between Neuber's method and the energy-based approach [14]

Diving deeper into the mathematical formulation, Neuber's method is expressed as :

$$K_i^2 = K_\sigma K_\epsilon = \frac{\sigma_N}{S_n} \cdot \frac{\epsilon_N}{e_n}, \tag{3.36}$$

Simplifying further to put the local stress-strains on one side :

$$\sigma_N \epsilon_N = K_t^2 \left(S_n e_n\right). \tag{3.37}$$

Figure 3.3 demonstrates how the different approaches evaluate stress-strain fields in the elastic-plastic region. Neuber's method does not integrate the area under the curve to determine the true stresses and strains but instead approximates these values. In contrast, Glinka's energy-based approach incorporates the exact values derived from the stress-strain curve, as described by the well-known Ramberg-Osgood equation. This approach provides a more accurate representation of material behavior beyond the linear elastic limit compared to Neuber's method.

In the purely elastic regime, the strain-energy-density (SED) approach states that

$$\underbrace{\frac{\sigma_N^2}{2E}}_{\text{local SED}} = K_t^2 \underbrace{\frac{S_n^2}{2E}}_{\text{nominal SED}},$$

Also considering that :

$$\sigma = E\epsilon. \tag{3.38}$$

$$S_n = E\epsilon_n. \tag{3.39}$$

It can be clearly shown why Figure 3.3 gives the exact same results when comparing both Neuber's method and the strain energy method approach. Moving further when considering local plasticity Neuber's expression takes the following form :

$$K_t^2 \cdot \frac{S_n^2}{2E} = \frac{1}{2}\sigma_N\epsilon_N = \frac{\sigma_N}{2}\left[\frac{\sigma_N}{E} + \left(\frac{\sigma_N}{K}\right)^{1/n}\right], \tag{3.40}$$

In which it can be seen that the right hand side of the equation had been shifted away from the strain energy density since the strain energy density states that "local SED = $K_t^2 \times$ nominal SED". Here, both sides represent elastic strain-energy densities. In this region, Neuber's rule coincides with the SED approach.

Another notable difference between these approaches, which is not directly related to how each equation mathematically accounts for the elastic-plastic region, lies in the results produced by their respective formulations. Several studies have observed that Neuber's method tends to exaggerate local plastic strains [29]–[32]. Given that accurately describing the local plastic stress-strain field is the primary objective of this study, the energy-based approach was ultimately adopted.

3.2.5. Extended Elastic Model for Post-Yielding Analysis at a Weld Toe

In this section, the upper limit of the analytical solution will be presented, extending den Besten's formulation Equation 3.1 to analyze stress distribution around a weld toe beyond yielding [11]. This approach considers both the pre-yielding and post-yielding regions of the material's stress-strain curve elastically. The consideration of upper and lower bounds adds an extra layer of validation to the analytical approach.

Den Besten's formulation [11], based on fully elastic material properties (Section 3.2.1), provides a theoretical framework for understanding the maximum possible stress concentration at the weld toe under idealized elastic conditions. While this formulation inherently leads to a highly exaggerated stress-strain response due to its exclusion of inelastic material behavior, incorporating inelastic properties allows for a more realistic representation of stress damping post-yielding. Which is why this extended elastic stress field will be considered to be the upper bound of the verifying equations.

The fully elastic stress-strain field, as derived from Equation 3.1, considers three key parameters: geometry, far-field stress, and weld load-carrying stress. Elastic material properties are implicitly included in the equation to comprehensively depict the stress distribution. The results of this extended fully elastic analysis will be presented in Section 3.3 to illustrate its application and implications.

3.2.6. Irwin's Stress-Strain Field Around a Weld Toe

The lower bound of the is determined using Irwin's method, which assumes an elastic perfectly plastic stress-strain behavior. The elastic perfectly plastic stress-strain model features a linear slope in the elastic region until the material reaches the yield point. Beyond this point, the material exhibits inelastic behavior characterized by a tangent modulus that is constant and equal to zero at every point in the inelastic region. This corresponds to a horizontal slope on the stress-strain curve. The behavior is illustrated in Figure 3.4.

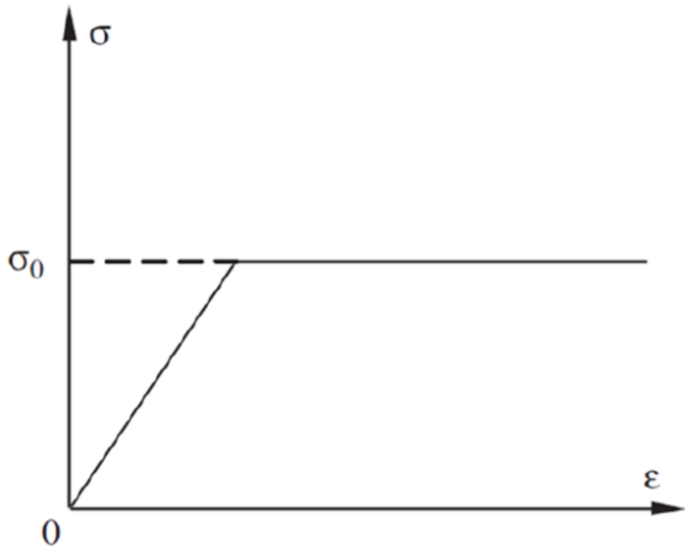

Figure 3.4: Elastic-Perfectly Plastic Stress-Strain Curve based on Irwin's method [27].

In this model, σ_0 represents the yield limit, which defines the maximum stress the material can sustain. As the material does not exhibit strain hardening, the inelastic region is characterized by a constant stress, resulting in the horizontal slope observed in the curve, i.e the stress is capped at the proportionality limit.

Irwin's method assumes the following relationship:

$$\sigma_y * r_p = \int \sigma dr \tag{3.41}$$

Here, r_p represents the size of the plastic zone. Solving for r_p provides:

$$r_p = \frac{1}{\sigma_y} \int \sigma dr \tag{3.42}$$

This formulation relates the size of the plastic zone to the parameters already defined and identifies the limit at which the stress-strain field is capped. Subsequently, the plastic field is determined by solving based on the previously established linear elastic stress-strain field introduced by den Besten [11], substituting it for σ in Equation 3.41. Once the plastic zone is identified, a corresponding plastic stress-strain field is formulated. This formulation caps the stress value beyond the yield limit at the point where the stress equals the specific value at the tip of the plastic zone, as calculated using r_p.

3.3. Results

This section presents the analytical stress field results near the weld toe and evaluates them against two reference models representing bounding conditions. These reference models define the upper and lower bounds of material behavior: the upper bound assumes a fully elastic response, while the lower bound incorporates a perfect elastic–plastic material behavior. To assess the validity of the adopted analytical method, a comparative analysis is carried out between the proposed model and these two bounding cases. The comparison is visualized in a single graph, illustrating the stress distribution in MPa as a function of the normalized position along the base plate thickness (i.e., position divided by total base plate thickness).

This approach allows for a comprehensive evaluation of the stress–strain behavior near the weld toe and helps establish confidence in the proposed method's predictive capabilities by confirming that it consistently falls within physically realistic boundaries.

Material Model

For consistency and clarity throughout this thesis, the same material and geometric configurations are used in both the analytical and numerical models. The materials considered are S690QL and AH36 steels. Their engineering stress–strain curves, derived from experimental data, are shown in Figure 3.5a and Figure 3.5b.

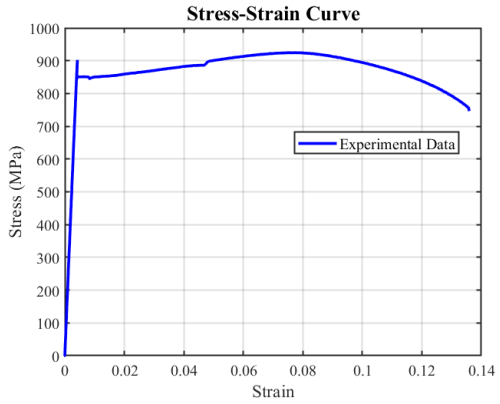

(a) Engineering stress–strain curve from experimental data for S690QL steel

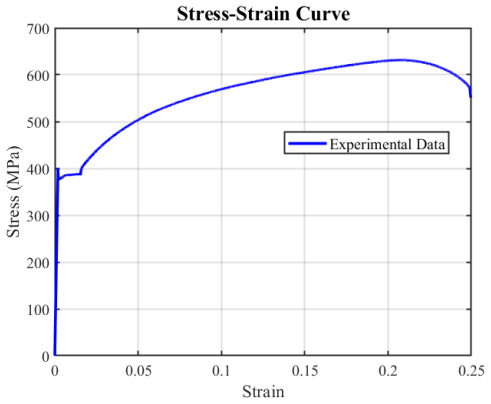

(b) Engineering stress–strain curve from experimental data for AH36 steel

The experimental data were sourced from Wei Jun et al. [26]. Since Glinka's strain energy density (SED) method requires the true local stress–strain relationship, the Ramberg–Osgood equation was considered, curve fitting was applied to approximate the material constants K and n. The fitted Ramberg–Osgood form is expressed as:

$$\epsilon = \frac{\sigma}{E} + \left(\frac{\sigma}{K}\right)^{1/n} \tag{3.43}$$

Initially, significant discrepancies were observed between the analytical stress–strain representation (using the Ramberg–Osgood law) and the experimental data. For S690QL steel, the average discrepancies between both post yielding were 7.19%, while for AH36 steel, it reached approximately 28%.

Despite these limitations, the Ramberg–Osgood model was adopted for both materials in the analytical analysis to maintain methodological consistency with the SED approach.

Geometry of the Model

Moreover, the same geometric configuration is used for both the analytical and numerical models. The joint considered is a Partially Penetrated Double-Sided (PPDS) T-joint, a common type of welded connection. The geometry is shown in Figure 3.6.

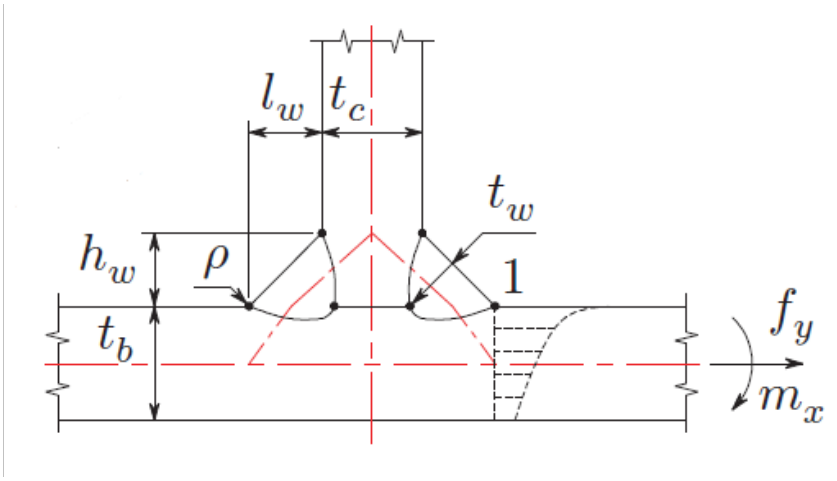

Figure 3.6: DSPP T-joint with asymmetric thickness in the base plate, as considered in this study [11].

The key dimensions of the model are summarized in Table 3.1.

Table 3.1: Geometric dimensions of the PPDS T-joint

Symbol	Description
tb	Thickness of the base plate: 100 mm
tc	Thickness of the central plate: 100 mm
hw	Height of the weld: 100 mm
lw	Width of the weld: 100 mm
l	Length of the weld: 1000 mm
ρ	Radius of curvature at the weld toe: 0 mm

3.3.1. Linear Fully Elastic Solution - Upper Bound

The linear elastic solution considers only the equation as proposed in Equation 3.1 but exaggerates and extends it to the point of failure, even though it is only true up to the proportionality limit. This approach typically overestimates the stress and strain behavior and is, therefore, used as the upper bound. The provided information includes the stress concentration factor across the base plate thickness, where the ratio $\frac{r}{t_b}$ is plotted to describe the considered location along the base plate. As $r \to 0$, the position closest to the weld toe is indicated, which is expected to be the most critically stressed location. Moving further away from the weld toe, as $r \to 1$, the ratio $\frac{r}{t_b} \to 1$ represents locations further along the base plate.

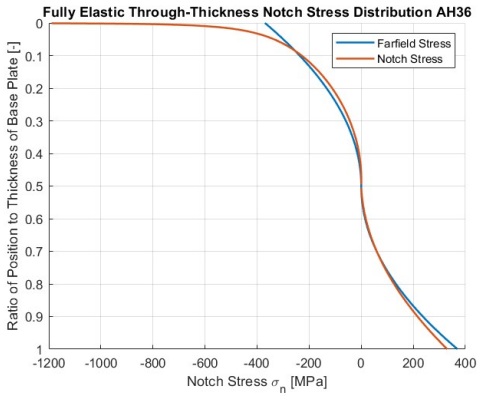

(a) Elastic notch stress (σ_n) along the thickness of base plate through thickness for AH36 steel due to pure bending

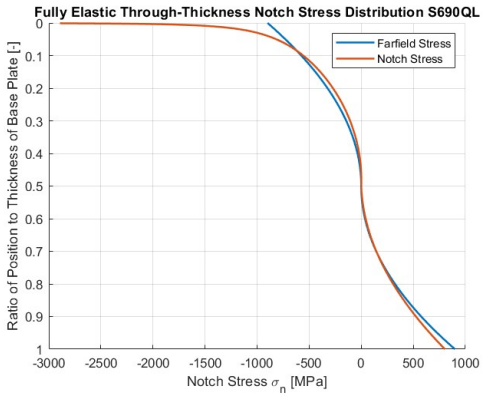

(b) Elastic notch stress (σ_n) along the thickness of base plate through thickness for S690QL steel due to pure bending

Figure 3.7: Elastic notch stress (σ_n) along the thickness of the base plate around a weld toe due to pure bending

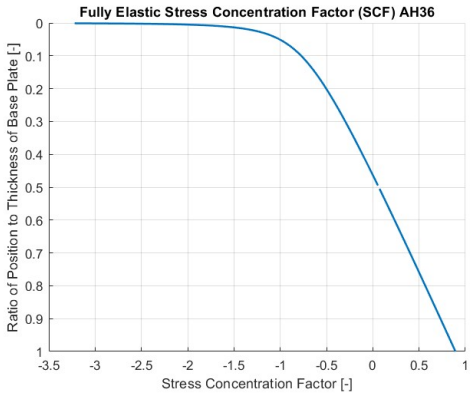

(a) Elastic stress concentration (SCF) along base plate for AH36 steel

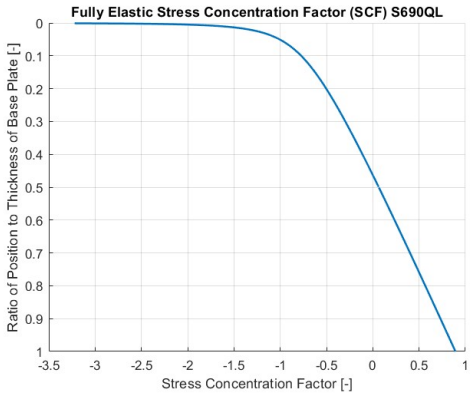

(b) Elastic stress concentration (SCF) along base plate for S690QL steel

Figure 3.8: Elastic stress concentration factor (SCF) along the thickness of the base plate around a weld toe

The results are based on a pure bending case, where the structural bending ratio $r_s = 1$.

3.3.2. Elastic–Perfectly Plastic Solution - Lower Bound

As referenced earlier in Section 3.2.6, Irwin's method assumes elastic–perfectly plastic material behavior. Under this assumption, the maximum stress is capped at the yield strength, with no strain hardening. Any stress beyond the yield point is entirely absorbed by plastic deformation, making it a conservative model often used for initial plastic zone estimates.

In this section, results are presented for the two materials: the high-strength steel (S690QL) and the lower-strength structural steel (AH36). The analysis focuses on the stress distribution along the base plate thickness of the welded joint.

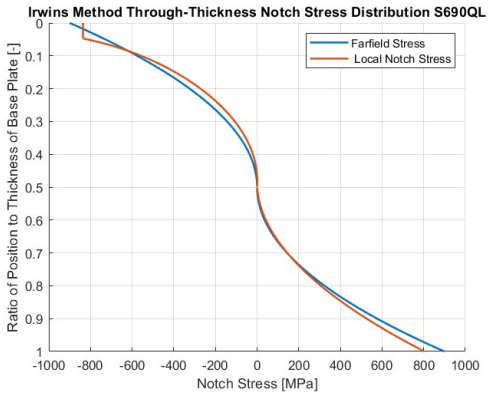

(a) Notch stress (σ_n) along the thickness of the base plate around a weld toe due to pure bending for S690QL steel

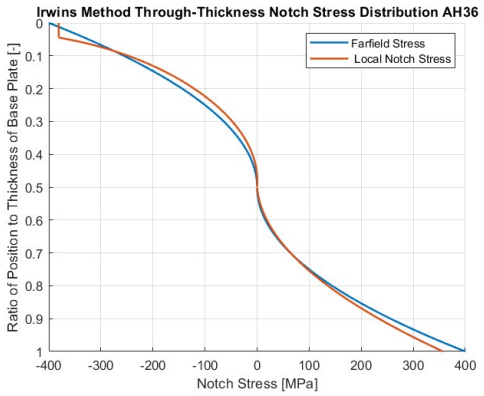

(b) Notch stress (σ_n) along the thickness of the base plate around a weld toe due to pure bending AH36 steel

Figure 3.9: Notch stress (σ_n) distribution at the weld toe based on Irwin's method for S690QL and AH36 steels

The capped stress predicted by Irwin's method defines the onset of first-order plastic deformation. This region is found to be highly localized at the weld toe, extending approximately 5% of the base plate thickness for AH36 steel. For the higher-strength S690QL, the plastic zone is even more confined, due to its higher yield strength and lower plastic strain capacity under the same loading conditions.

3.3.3. Strain Energy Density Approach

After introducing the upper and lower bounds for the transitioned analytical solution in the previous sections, this section will present the results of the final and adopted approach. Additionally, the subsequent section of this chapter will briefly discuss the differences among the three results—upper bound, lower bound, and the transitioned adopted solution—and evaluate whether the results exhibit a consistent and expected pattern.

As with the previous analyses, comparisons will be made for both S690QL (a high-strength steel, HSS) and AH36 (a lower-strength steel). The main parameter of comparison will include the distribution of the stresses along the width of the base plate for both materials. These comparisons will follow the methodology and parameters outlined in earlier sections.

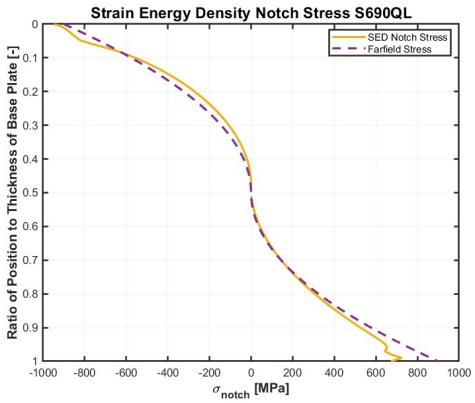

(a) Notch (σ_n) and Farfield stress (σ_f) distribution due to pure bending along the thickness of base plate for a weld toe considering S690QL steel

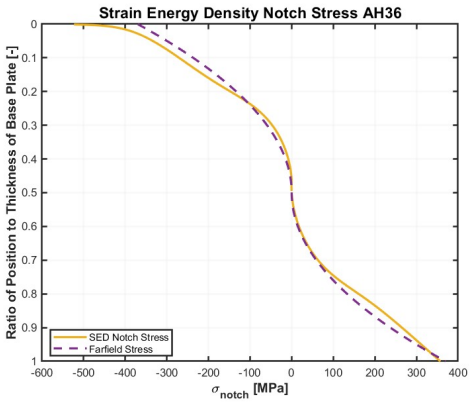

(b) Notch (σ_n) and Farfield stress (σ_f) distribution due to pure bending along the thickness of base plate for a weld toe considering AH36 steel

Figure 3.10: Values of the notch stress (σ_n) and farfield stress (σ_f) along the thickness of the base plate at the weld toe for T-joint based on Glinka's approach (SED method)

3.4. Verification and Discussion

The results from the three different analytical stress-strain fields yielded highly positive and expected outcomes. As anticipated, the linear fully elastic results, when extended into the inelastic region, were significantly exaggerated due to their failure to account for plasticity or inelastic material behavior. In contrast, the elastic-perfectly plastic method, acting as the lower bound, demonstrated capped stresses once the plastic zone was entered, without exhibiting strain hardening, as previously explained. The energy-based method produced results that were bounded between these upper and lower ranges, effectively capturing the transitional behavior. These findings are illustrated in Figure 3.11.

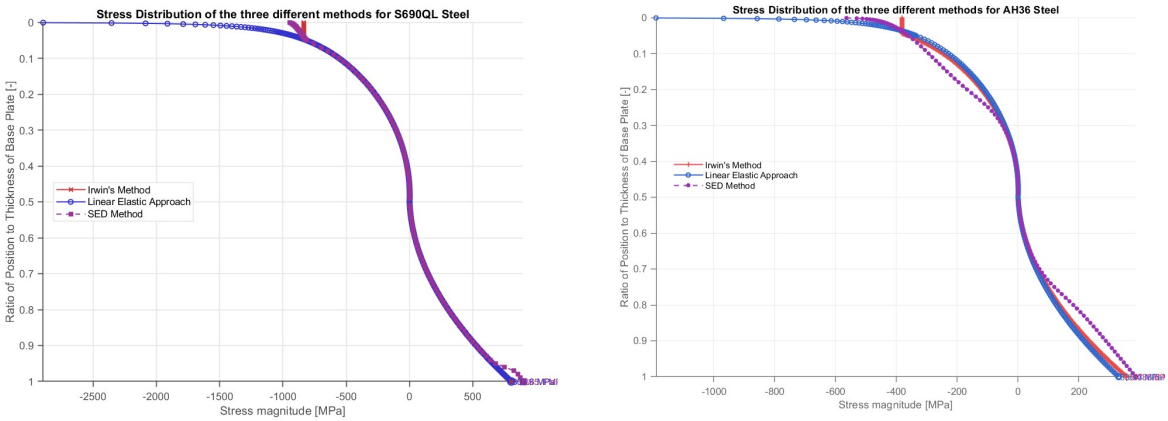

(a) Stress distribution comparing the different analytical approaches to verify the adopted analytical method for S690QL steel.

(b) Stress distribution comparing the different analytical approaches to verify the adopted analytical method for AH36 steel.

Figure 3.11: Stress distribution comparing the different analytical approaches to verify the adopted analytical method for S690QL and AH36 steels

These comparisons and positive results provide an initial indication that using strain energy densities as a transitioning method performs as expected. Further discussions and final validation will be presented in Chapter 4 with the numerical model. However, some differences are anticipated due to various assumptions inherent in the analytical model. For instance, the model assumes that stresses and strains are highly localized, allowing the relation:

$$W_S = W_\sigma \quad \text{or} \quad \int_0^{e_{ij}} S_{ij}\, d\epsilon_{ij} = \int_0^{\epsilon_{ij}} \sigma_{ij}\, d\epsilon_{ij}. \tag{3.44}$$

4

Numerical Model

4.1. Numerical Model

This chapter presents a detailed description of the numerical model developed for this study as validation for the main analytical model. The numerical model was implemented using ANSYS APDL Mechanical Enterprise Academic Research, 2022 R2, a Finite Element Analysis (FEA) software package. The numerical approach outlined here aims to validate the results obtained from the analytical model expressions in the previous chapter. Each section in this chapter corresponds to different criteria used to configure the numerical model.

4.2. FEA Considerations & Errors

This section provides insight into key considerations in finite element analysis (FEA). In this case, the primary factors are discretization errors and numerical errors.

- **Numerical errors** arise from computational issues, such as rounding errors or unstable algorithms that fail to converge during iterative solutions. These errors are common in all numerical models but are particularly relevant when dealing with highly localized areas due to detailed measurements. In such cases, rounding errors or other algorithmic inaccuracies can affect the results.
- **Discretization errors** stem from both the type of elements used in the model and the characteristics of the mesh. An excessively fine mesh in areas with sharp corners can lead to unrealistic, unbounded stress values, whereas an overly coarse mesh may fail to accurately capture local structural behavior. In this case, the geometric structure involves a weld toe (i.e., a sharp V-notch), which presents challenges in optimizing mesh size. Increasing the number of elements and refining the mesh can improve accuracy but also significantly increase computational time. Therefore, errors associated with unbounded stresses in numerical models are particularly relevant and are expected to impact the results.

4.2.1. Mitigation Strategies

Since these errors can cause discrepancies between simulation results and analytical expectations, mitigation strategies were implemented, including:

- Validation and verification techniques to ensure the model behaves as expected under identical loading conditions and geometric properties.
- Conducting convergence studies by refining the mesh or adjusting time steps to improve result accuracy. In this case, a mesh density convergence technique was used to ensure results remained within specified bounds.

4.3. The Numerical Framework

The same considered structure as in the previous chapters will also be considered in the numerical model. The T-Joint is subjected to Mode I loading, with stresses expected along the thickness of the base plate. However, for simplicity, an L-Joint is analyzed, by making use of symmetry along the YZ plane in this case. As a result, the L-Joint is modeled as a 2D structure under plane strain conditions, with no deformation along the out-of-plane direction. Since the T-Joint is represented as a 2D structure in the x-y plane, deformation along the z-axis is assumed to be zero, expressed mathematically as $\epsilon_z = 0$.

The primary objective of the numerical analysis is to validate the main analytical expression discussed in the previous chapter. While the geometry of the L-Joint remains unchanged, two materials will be considered: S690QL and AH36. Additionally, the loading conditions will also be the same for both materials, where the load will be based on pure bending clockwise around the z-axis. The following sections provide a detailed explanation of the criteria and configurations employed in the numerical method.

4.3.1. Elements

The primary objective is to characterize the stress fields around weld toes for high-strength steels beyond the elastic limit, necessitating the use of an element that aligns with the model's criteria. In this study, the PLANE182 element was selected as the most suitable. Only one type of element was used since the objective of the study was to analyze the configuration of the welded T-Joint rather than the material and mechanical properties of the weld. PLANE182 is a 2-D solid element with two translational degrees of freedom in the x and y directions. This element is designed to accommodate plasticity, large deflections, and large strain capacities, all essential for this analysis.

Table: Plane 182 Structural Features

Feature	**Description**
Element Type	2D Structural Solid (PLANE182)
Nodes	4 nodes (quadrilateral) or 3 nodes (triangular). Supports mid-side nodes for quadratic behavior.
Degrees of Freedom	Translational (UX, UY)
Applications	Used for 2D structural analysis, including linear, nonlinear, and thermal-structural coupling.
Plasticity	Supports isotropic and kinematic hardening plasticity models.
Stress Stiffening	Yes, supports stress stiffening effects for geometrically nonlinear analysis.
Large Strain Behavior	Supports large deformation analysis with nonlinear material properties.
Element Shape	Quadrilateral (4-node), Triangular (3-node) shapes.
Nonlinear Capabilities	Handles large strain, large displacement, and nonlinear material properties.

Key Option	**Description**
K1: Integration Option	**1 (Reduced Integration)**: Reduced integration is used to avoid shear locking in bending-dominated problems.
K3: Plane Stress/Strain Option	**2 (Plane Strain)**: Plane strain is used for thick 2D structures where out-of-plane deformation is negligible.
K6: Mixed Formulation Option	**0 (Pure Displacement)**: Pure displacement formulation is the default and suitable unless dealing with nearly incompressible materials.

4.3.2. Material Model

The material model is a critical component in the numerical analysis, as this study primarily focuses on the post-yield behavior of high-strength steels (HSS) and how steels with lower strength respond under the same loading conditions and configurations. As stated in the previous section, a homogeneous material assumption is adopted, excluding the effects of material variation and the heat-affected zone (HAZ), which are beyond the scope of this study. The numerical model is based on experimental data provided by Wei Jun et al. [26], with additional approximations. Two types of steel are considered: S690QL, a high-strength steel, and AH36, a lower-strength steel [26]. The material properties for both steels are summarized in Table 4.1 below.

	E [GPa]	v [-]	σ_y [MPa]	$\epsilon_{sh,p}$ [-]	ϵ_0 [-]	K [MPa]	n [-]
S690QL	206.1	0.3	836	0.0438	0.0413	984.1	0.0192
AH36	208.8	0.3	381	0.0138	0.0077	794.0	0.0141

Table 4.1: Material properties for S690QL and AH36

The experimental specimens used in this study were identical for both AH36 and S690QL steels. The specimens, designed to account for transverse material properties, are shown in Figure 4.1.

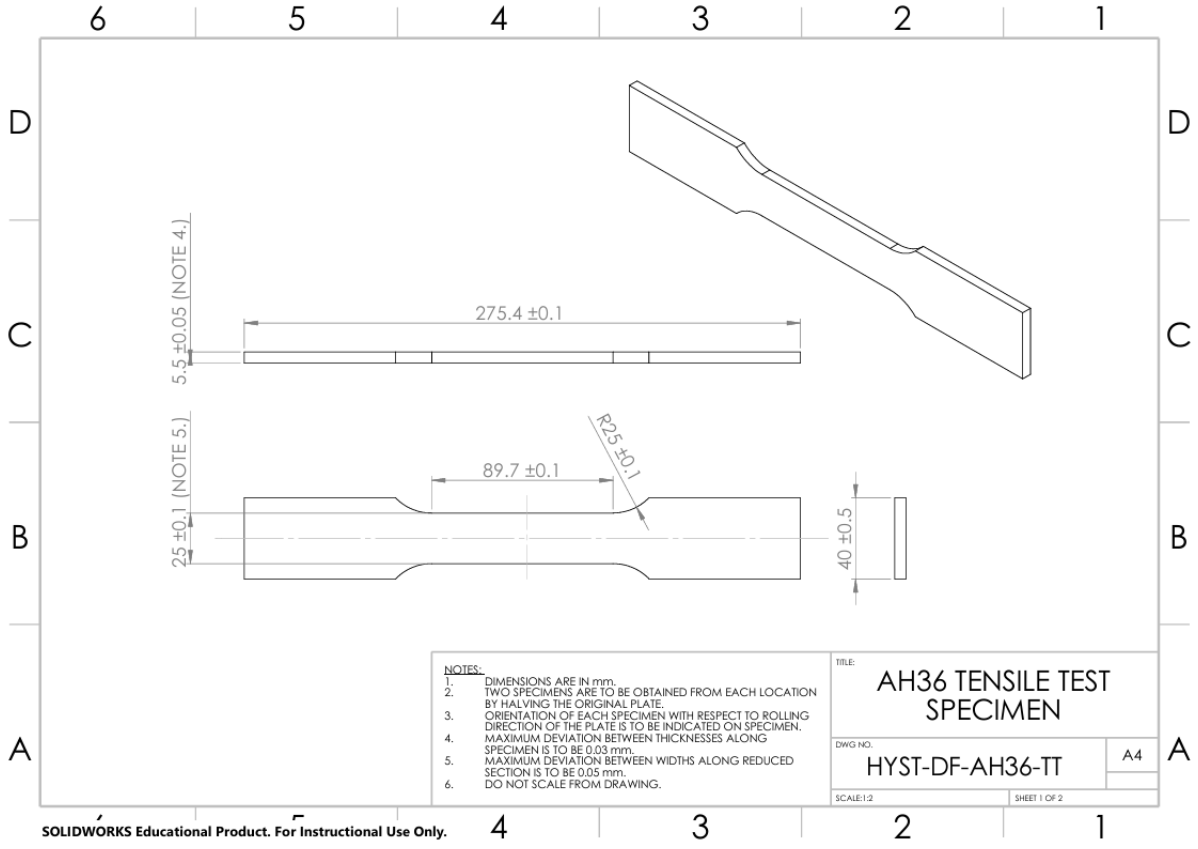

Figure 4.1: Dimensional drawing of the experimental tensile test specimen used for both AH36 and S690QL steels [26].

The dimensions of both specimens were determined in accordance with the standard sizes specified by ship classification rules. ANSYS utilizes various inelastic material models, particularly those incorporating plasticity, to accurately represent stress-strain behavior beyond the yield point, which is a primary focus of this study. In this context, the most suitable inelastic material model was identified as the multilinear plasticity hardening model, which allows up to 100 data points to describe the post-yield stress-strain behavior.

The main limitation of this model is that it does not permit the input of a fully detailed material model but rather a generalized stress-strain curve sample beyond the yield limit. Since 100 points beyond the elastic limit were considered, true stresses and plastic strains were required as input for ANSYS. Specifically, for this material model, beyond the elastic properties provided in Table 4.1, the experimental values for both materials had to be converted from engineering stresses and strains into the required format to ensure ANSYS correctly accounts for plastic behavior. Consequently, the engineering values presented by Wei Jun et al. were converted into true stress and plastic strain using the following relationships:

$$\epsilon_{true} = \ln(1 + \epsilon_{eng}) \tag{4.1}$$

$$\sigma_{true} = \sigma_{eng} \cdot (1 + \epsilon_{eng}) \tag{4.2}$$

$$\epsilon_p = \epsilon_{true} - \frac{\sigma_{true}}{E} \tag{4.3}$$

Furthermore, to comply with the 100-point limitation imposed by ANSYS, a sampling process was conducted to ensure an accurate representation of the material behavior. The selected 100-point dataset was carefully chosen to capture the stress-strain response between the yield point and the ultimate tensile strength. The following Figures 4.2a and 4.2b illustrate the resulting stress-strain curve after the sampling process, using the 100 chosen points to describe the plastic behavior of the material.

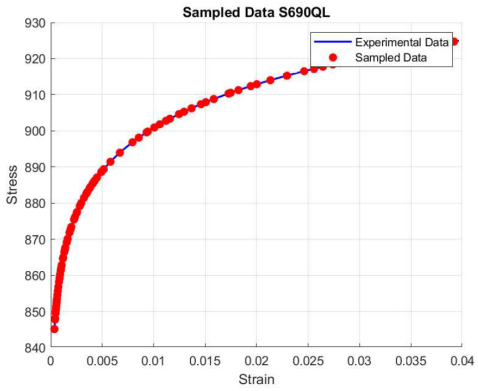

(a) Stress–strain data sampled from the experimental results for S690QL steel.

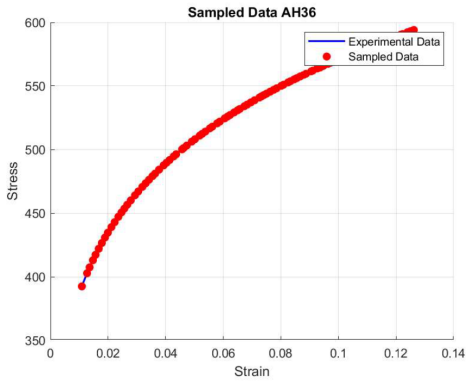

(b) Stress–strain data sampled from the experimental results for AH36 steel.

Figure 4.2: Sampled post-yield stress–strain data up to the ultimate tensile strength for both the S690QL and AH36 steels based on experimental results.

It is evident from the figure above, and generally expected, that AH36 steel exhibits a smoother and more ductile response compared to S690QL, which demonstrates a sharper transition post-yielding. Due to the significant strain-hardening properties of AH36 steel, the Ramberg-Osgood equation is expected to describe its stress-strain curve less accurately than that of S690QL due to its formulation. Consequently, discrepancies may arise between the analytical model, which utilizes the Ramberg-Osgood equation, and the numerical model, which relies on experimental stress-strain data.

4.3.3. Model Geometry and Dimensions

Since a 2D PPDS T-Joint can be simplified by assuming symmetry in the YZ plane at $x = 0$, the model was limited to an L-Joint after symmetry to account for any reaction forces. Cartesian coordinates were considered, with the local structural origin also being the global origin of the model, as visualized in the figure. The model was 1 meter in the x-direction, with a sharp notch; in other words, $\rho = 0$, the localized and most stressed region, potentially causing unbounded stresses.

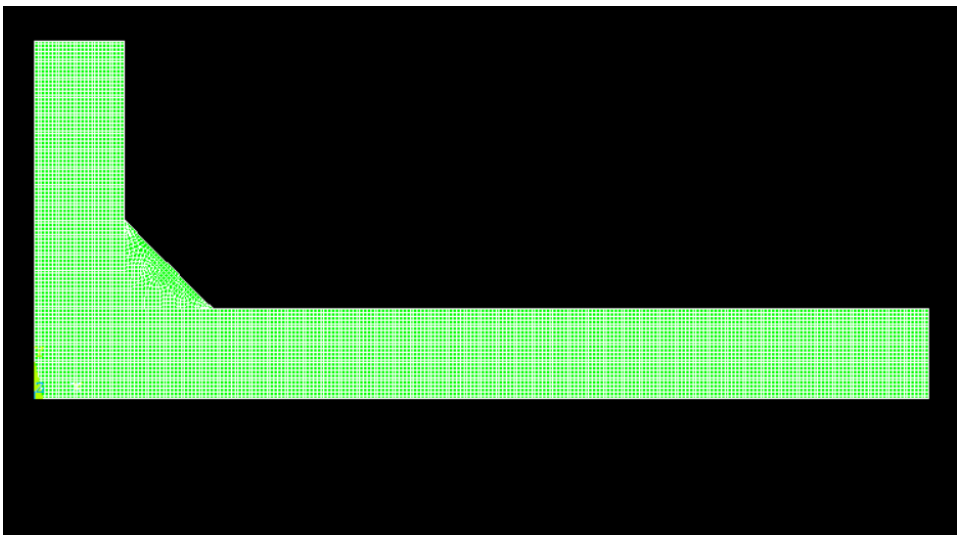

Figure 4.3: Finite element model of the global structural geometry showing mesh discretization used for numerical simulation.

4.3.4. Mesh

In this case, the weld toe forms a sharp V-notch, making the region highly sensitive to stress variations. As stress transitions from the continuous area to the notch, careful mesh selection is crucial for achieving accurate results. However, while a finer mesh improves accuracy, it also increases computational time, necessitating a balance between refinement and efficiency. The mesh, element size, illustrated in Figure 4.4a, was globally set to 0.04 mm, providing reliable results within a reasonable computational time. Mesh convergence was assessed using mesh density convergence, specifically around the weld toe, by analyzing the peak expected stress for different element sizes until convergence was observed. To enhance realism, model continuity was ensured by merging elements and nodes with a maximum tolerance of 0.0001 mm. This step was essential to prevent artificially high stress concentrations, particularly in refined areas where geometric changes occur locally in the structure between different modeled areas.

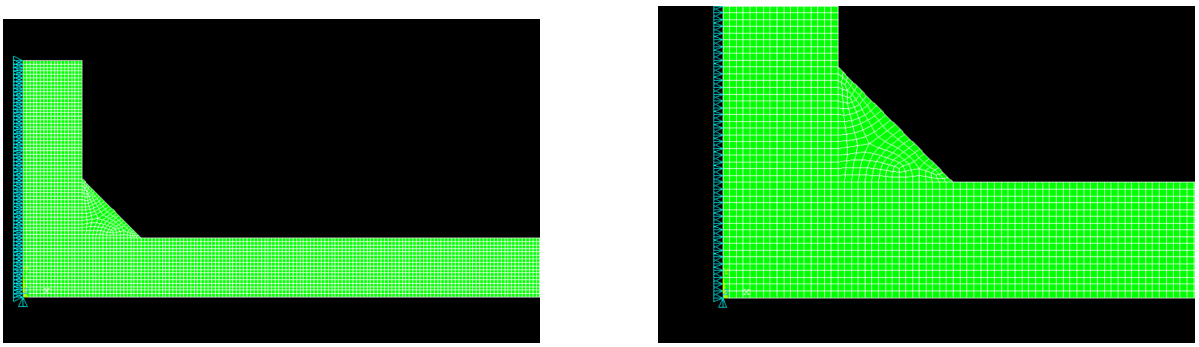

(a) Global mesh of the full structural domain.

(b) Refined mesh near the weld toe, ensuring continuity across regions with geometric transitions.

Figure 4.4: Mesh configuration applied to the PPDS T-joint model, highlighting both global and localized refinement strategies.

4.3.5. Boundary Conditions

The boundary conditions for the numerical model, specifically for FEA, are used to approximate the true physical behavior of the structure. While it is impossible to replicate the exact physical behavior, the following section illustrates the chosen boundary conditions and the rationale behind them. At $x = 0$, the displacement in the x-direction (UX) was restricted to enforce symmetry, as the geometry is based on an L-Joint derived from a PPDS T-Joint. As previously discussed, symmetry boundary conditions were applied to the model, assuming symmetry of the T-Joint with respect to the Y-Z axis to ensure any reaction forces or displacements possible due to the availability of the other side of the T-Joint. The displacement in the x-direction was also restricted at the left end of the L-Joint, as shown in the following figure:

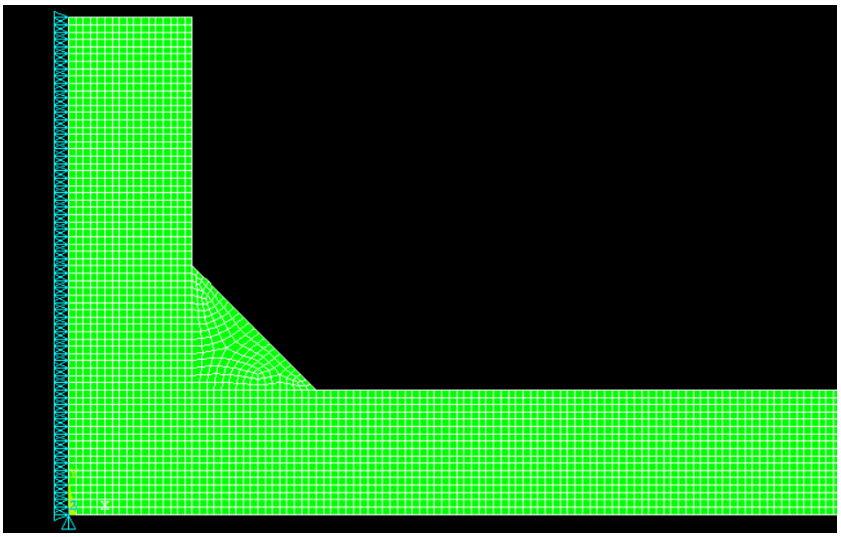

Figure 4.5: Symmetry boundary condition applied along the vertical edge of the model, constraining horizontal displacement ($U_X = 0$) to simulate half-geometry behavior.

The point of origin for the model was set at coordinates (0,0). Since the model is considered two-dimensional (2D), the displacement in the x-direction (UX) was restricted, as well as the displacement in the y-direction (UY) only at the point of origin. This setup is illustrated in the following figure:

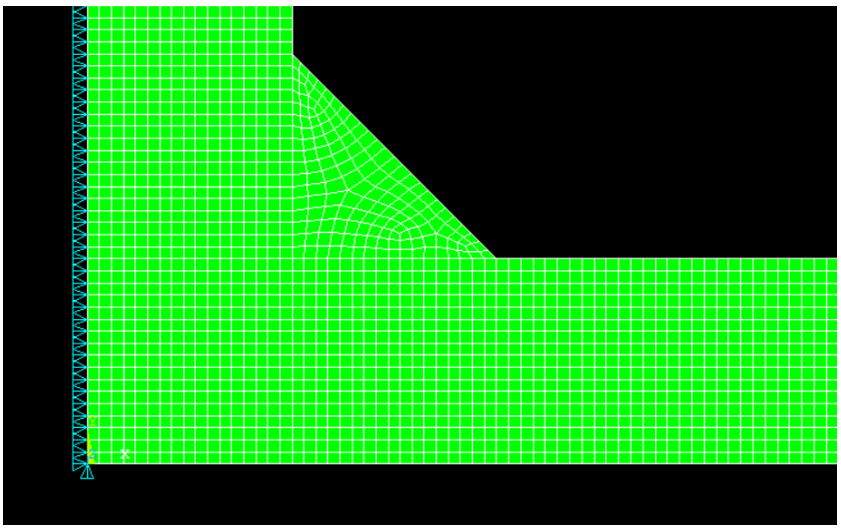

Figure 4.6: Applied boundary condition at the origin, constraining both horizontal and vertical displacements ($U_X = 0$, $U_Y = 0$) to eliminate rigid body motion and ensure simulation stability.

The constrained displacement in the y-direction ($UY = 0$) at the origin ensures that the model remains

fixed and establishes the origin point. Without this constraint, the model would shift under applied loads. Additional physical boundary conditions were not included because they are unnecessary and could introduce high residual stresses when considering mechanical weld properties. Since mechanical weld properties are not accounted for in this study, avoiding additional boundary conditions further simplifies the analysis, even for possible further studies.

4.3.6. Applied Loads

Mode-I loading is considered for this structure, as discussed in previous chapters. This loading condition is expected to generate the highest stresses around the weld toe along the base plate of the T-joint. Consequently, the analysis focuses on an HS Type C stress distribution, where the sharp V-notch at the weld toe is anticipated to yield first.

Pure bending was applied to the model by setting a varying pressure on the right end of the model (the free end of the base plate) to create a clockwise moment about the z-axis. In other words, the structural bending ratio (r_s) is 1, meaning the ratio between the bending stress and the structural stress is unity.

To directly apply a bending moment in ANSYS, a 3D element is typically required. However, since the PLANE182 element (a 2D element) is used, two methods for simulating a moment were considered: (1) applying a multi-point constraint (MPC), or (2) using a more straightforward and simpler approach by applying a pressure along the thickness of the base plate. The latter approach involves varying the pressure along the thickness to induce a bending moment about the z-axis and was used.

The applied loads were aligned with those used in the analytical model to ensure consistency in validation. The load values were selected to capture plasticity effects and the material behavior beyond yielding.

The following sections present graphical and visual results for the numerical model, which are compared to the proposed analytical method for validation. The differences between both methods are critically evaluated, along with an assessment of any discrepancies in the numerical results.

4.4. Results

In this section, the numerical model results are presented as both graphical plots and contour plots to provide a detailed visual representation of the stress distribution along the thickness of the base plate. All results are given as the X-component of stress along the ratio of the position of the base plate thickness, as used for the transitioned analytical model. The stress values were extracted from nodes around the notch along the base plate thickness for both S690QL and AH36 material models.

The contour plot is provided below to visualize the X-component of stress [MPa] throughout the base plate, illustrating both the overall stress distribution due to pure bending and the localized stress concentrations along the thickness of the base plate. For both cases below, in Figures 4.7 and Figures 4.8 the local and global reactions of the structure are illustrated with a legend at the bottom to identify the values of the X-component of stress in MPa along the base plate.

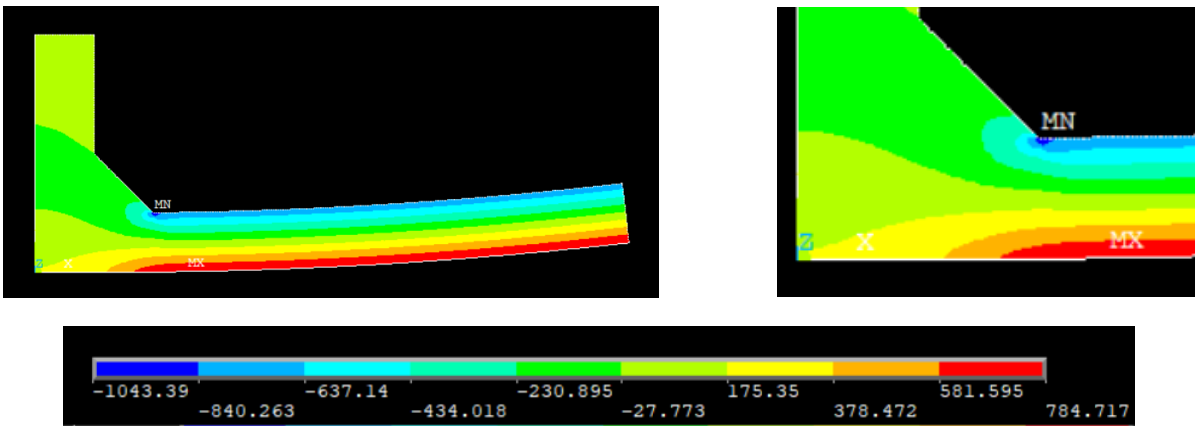

Figure 4.7: X-component of stress distribution in MPa due to pure bending on an L-joint for S690QL steel along the thickness of the base plate

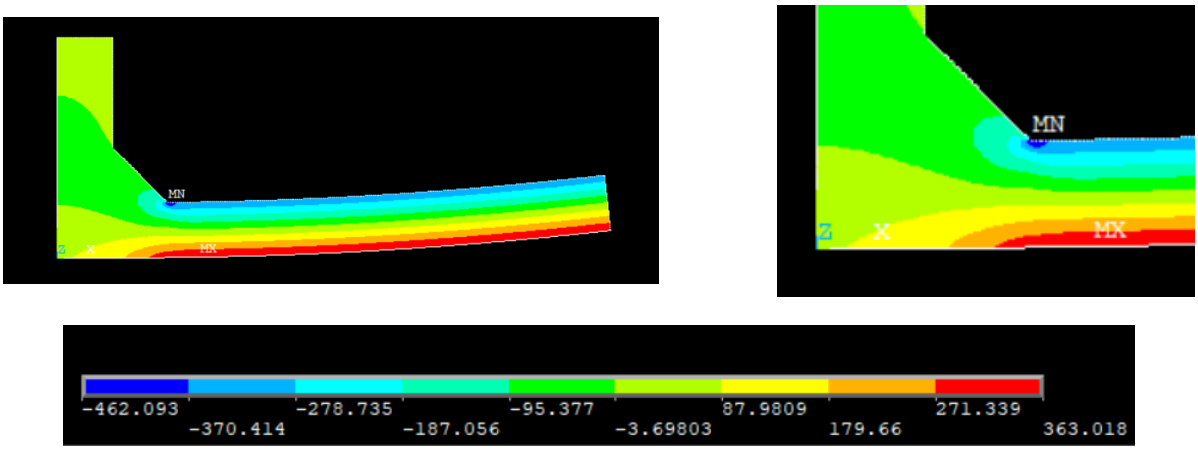

Figure 4.8: X-component of stress distribution in MPa due to pure bending on an L-joint for AH36 steel along the thickness of the base plate

For both cases, as expected, the highest stresses were observed in the vicinity of the weld toe, away from the regions where the loads were applied. This result aligns with expectations based on the structural configuration and loading type.

After extracting the numerical results, a final validation of the analytical model is necessary. The reasons behind the differences in values obtained from each model will be analyzed in the following section. Additionally, a conclusion will be drawn on how the results and methodologies of both models influenced the study.

4.5. Validation and Discussion

After verifying the analytical model against established analytical approaches, a finite-element (FE) model was developed in ANSYS to provide an independent validation of the results. This section compares the FE predictions with those obtained from the analytical formulation. Figures 4.9 and 4.10 demonstrate that the Strain Energy Density (SED) method proposed by Glinka reproduces the X-component of stress from the FE model with good accuracy in the highly stressed region adjacent to the weld toe. For consistency, the numerical results are plotted using the same axis scaling as the analytical solution. In both figures, the ordinate represents the normalized through-thickness coordinate r/t_p, where $r/t_p \to 0$ corresponds to the weld toe and $r/t_p \to 1$ to the outer surface of the plate.

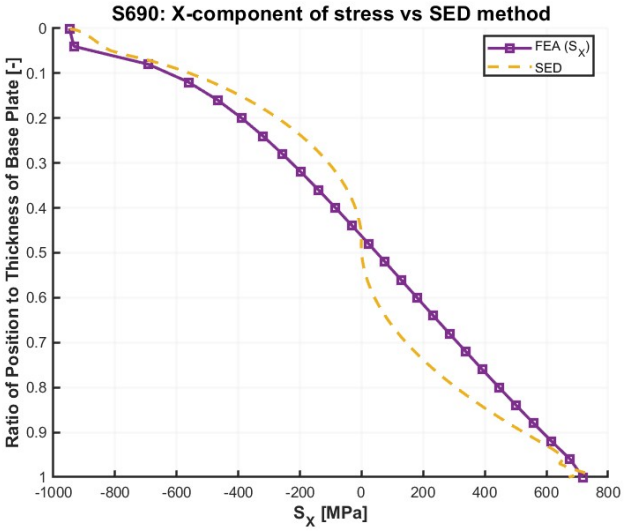

Figure 4.9: Stress–distribution comparison between FE (X-component of stress) and the SED analytical model for S690QL steel under pure bending.

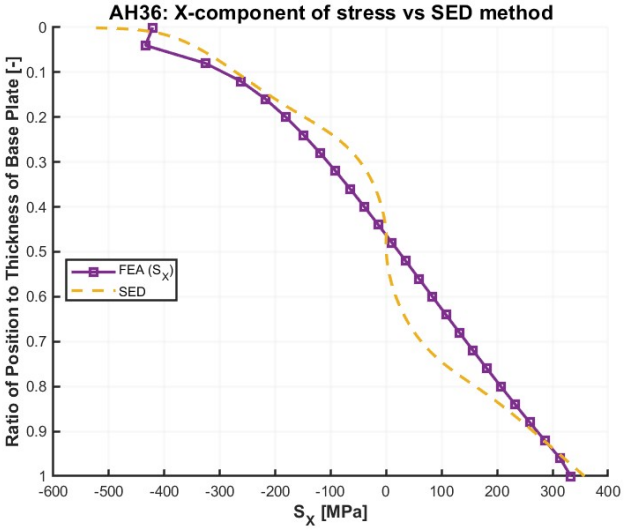

Figure 4.10: Stress–distribution comparison between FE (X-component of stress) and the SED analytical model for AH36 steel under pure bending.

Both models exhibit the same qualitative trend; however, the analytical curve is shifted relative to the finite element (FE) results, particularly near the neutral axis. This discrepancy is most likely attributed

to the material model description—specifically, the Ramberg-Osgood equation—and the experimental material data used for the numerical model.

The analytical model, does not consider the shear component of stress. However, it contributes significantly to the overall equivalent stress distribution as illustrated in Figures 4.11 and 4.12 from the FE model. Although this shear stress contributes significantly to the overall equivalent stress distribution, it is not accounted for in the analytical model, which primarily considers the X-component of stress. This is the second only significant contribution to the overall stress distribution. Nevertheless, the X-component part of the distribution gives an adequate representation of the overall structural behavior by focusing on the dominant stress components. Future work could simply consider both the shear stress τ_{xy} and the X-component of stress, making a very representative contribution to the total equivalent stress of real-life structural behavior.

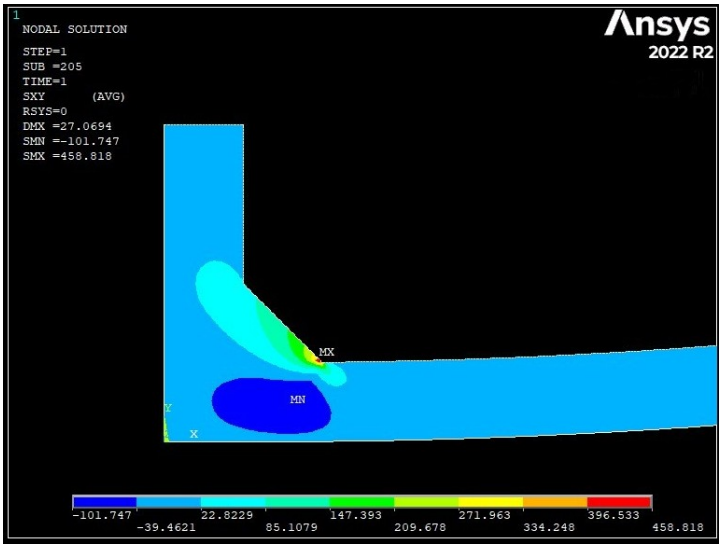

Figure 4.11: Distribution of τ_{xy} along the L-joint predicted by ANSYS for S690QL steel under pure bending.

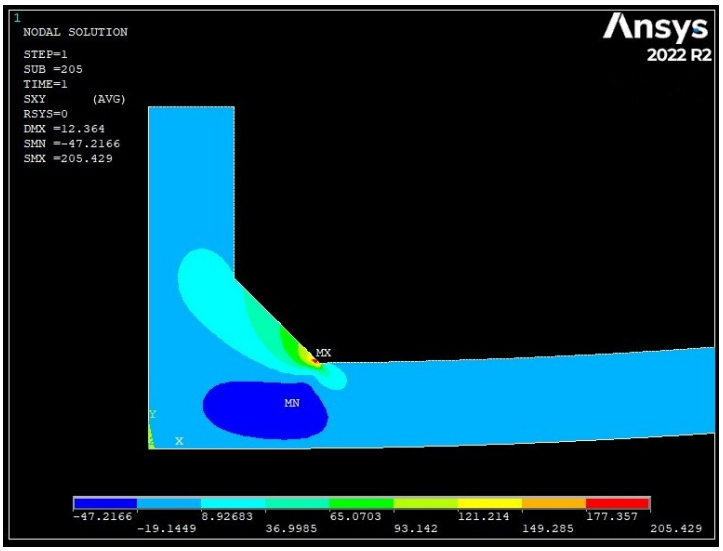

Figure 4.12: Distribution of τ_{xy} along the L-joint predicted by ANSYS for AH36 steel under pure bending.

As illustrated in Table 4.2, Glinka's approach demonstrates high accuracy in the region closest to the weld toe notch. The error percentage at the weld toe was about 3% for the higher strength steel and about 11% for the steel with the lower strength.

Material	FEA [MPa]	SED [MPa]	Error [%]
S690QL	977.894	946.624	3.3
AH36	386.427	431.017	11

Table 4.2: Direct quantitative comparison of FEA and Glinka's SED method results at the weld toe

5

Conclusions

Understanding the behavior of high-strength steels (HSS) in welded structures is a critical area of research, particularly due to its increasing adoption in demanding engineering applications. This thesis addressed the challenges of accurately predicting stress fields around weld toes analytically in the inelastic region, focusing on extending an elastic analytical methodology to account for post-yielding behavior. The central research question—"How can a general analytical expression be developed to describe stress fields in high-strength steels with post-yielding strain hardening in the vicinity of weld toes?"—was thoroughly examined through a combination of analytical modeling, numerical simulations, verification, and validation efforts.

After evaluating various potential analytical methodologies to address this question, Glinka's method was identified as the most relevant and was therefore utilized to model stress fields. The approach was first verified against other analytical methods and subsequently validated using a robust numerical model, yielding positive results. This, in turn, provides designers with an accurate and computationally efficient method for analyzing sensitive structures—in this case, welded joints with sharp notches lacking curvature, which result in stress singularities. The method has broad applicability, both in industrial practice and academic research. Academically, it opens up numerous opportunities for further research and possible refinement of the current analytical framework.

5.1. Analytical and Numerical Work

The foundational elastic analytical model, based on den Besten's formulation, was modified to extend its applicability into the inelastic region. The Strain Energy Density (SED) method was chosen over Neuber's well-known method and Stowell's generalized approach, resulting in an efficient and relatively accurate technique for analyzing highly localized features such as weld toes, V-notches, and cracks. The model captures localized plasticity while assuming the surrounding material behaves as fully elastic—striking a balance between computational efficiency and practical engineering application. This assumption holds when plasticity is highly localized; the more confined the plastic zone, the more dominant the surrounding elastic region becomes in governing the material's behavior. The method was initially verified against two analytical models representing the lower and upper bounds: Irwin's method and an extended linear elastic model, respectively. The SED method's results fell between these bounds after yielding, confirming its credibility. Irwin's method, which estimates the size of the first-order plastic zone, also offers a potential approach for defining the extent of the localized region using an elastic–perfectly plastic stress–strain relationship. The upper bound, on the other hand, extends the elastic solution to approximate structural behavior up to failure.

The numerical model was implemented using ANSYS and played a significant role in this study by validating the analytical results. The same geometry and material properties used in the analytical model were applied, as the primary goal was validation. The PP DS T-joint was numerically modeled as an L-joint, assuming symmetry in the YZ plane. Boundary conditions and loading scenarios were carefully selected to closely replicate the physical behavior observed in welded joints. These boundary

conditions accounted for both symmetry and the point of origin. The material model used true stress and plastic strain values derived from existing engineering stress data, using materials consistent with those in the analytical model. Mesh refinement was carefully managed to balance computational efficiency and accuracy, especially in regions with sharp stress concentrations.

The FE results showed good agreement with the SED predictions in the highly stressed region near the weld toe, particularly for the higher strength steel (S690QL), where the error was approximately 3%. For the lower strength steel (AH36), the deviation was higher, reaching 11%. The analytical method successfully reproduced the overall stress distribution trend and provided a conservative estimate. However, some discrepancies were observed in the overall trend. Despite this limitation, the validation confirmed that the SED approach remains a credible tool for capturing localized plastic effects while maintaining practical accuracy for engineering assessments. The analytical model, which forms the core of this study, was developed using a fitted stress-strain relationship based on the Ramberg-Osgood equation. Because the study involves two different materials—S690QL and AH36—the accuracy of the analytical model varied between them, particularly in the region near the weld toe. While both models showed generally good agreement with the numerical results, the differences in material properties led to variation in accuracy, especially in the yielding region. As demonstrated in earlier chapters, the Ramberg-Osgood equation provided a significantly better fit for the S690QL steel compared to the AH36 steel. Consequently, the analytical model exhibited higher accuracy for S690QL when compared to the numerical results, reinforcing the influence of the chosen material's stress-strain fit on the overall model performance.

5.2. Contributions and Practical Implications

This thesis contributes meaningfully to both academic research and practical engineering in the industry. On the academic front, it demonstrates the feasibility of using an energy-based approach—specifically the Strain Energy Density (SED) method—for analyzing localized stress in welded structures. It highlights the potential of this method to model stress concentrations at features such as weld toes and notches with reasonable accuracy. One promising area for future research is defining the limits of localized plasticity where Glinka's method remains valid. Irwin's method, used here for verification, could help estimate the plastic zone size and establish the boundary conditions under which Glinka's energy equivalence assumption holds. The study also prompts questions about how different material properties, geometries, and loading conditions influence localized stress behavior. While this thesis focused on a single loading case—pure bending—further work could explore additional load types, more complex joint geometries, and the inclusion of full weld mechanical properties to broaden the method's applicability. Another potential direction involves incorporating shear stress effects, which were the second and only most significant stress component effects on the total equivalent stress distribution. Extending the analytical model to account for shear would improve its completeness and predict a more real-life structural behavior. Practically, the proposed framework offers engineers a tool to design safer and more efficient structures by providing better insight into structural behavior and failure mechanisms. The findings are especially relevant to the construction and offshore industries, where high-strength steels (HSS) are widely used and stress hotspots often form in welded regions. Understanding the behavior of structures beyond the elastic limit—particularly whether failure is ductile or brittle—is critical for reliable design and safety assessments.

This study also acknowledges certain limitations, particularly in the underlying assumptions of the analytical approach. Although the method is not restricted to the Ramberg–Osgood equation and can accommodate various material models, its effectiveness depends on the specific material and its post-yielding behavior. In this regard, the Ramberg–Osgood model provided a more accurate representation of the stress–strain response for S690QL steel compared to AH36 steel. Furthermore, Glinka's method assumes that the yielding zone is highly localized, with the inelastic region governed predominantly by the surrounding elastic material. This assumption holds when plastic deformation is confined near the notch, as the elastic region dominates in both size and influence. However, when yielding extends beyond the immediate vicinity of the notch, the predictive accuracy of the model diminishes.

Additional limitations stem from the numerical method itself. Mesh refinement was optimized within the constraints of available time and computational resources. Although this resulted in a somewhat rounded outcome, a sufficient level of convergence was observed prior to finalizing the selected mesh

density, supporting the validity of the numerical predictions.

Future research should also consider the influence of additional factors such as residual stresses from welding and temperature effects. Since the only aspect that was mainly taken into account was the geometry of the weld and not the full mechanical properties of the weld, future studies can work further on giving a more realistic description of the models. On the numerical side, enhancements in meshing strategies and validation techniques could further improve simulation accuracy. Collaborative efforts between academia and industry may lead to more comprehensive, real-world applicable models. Lastly, future studies could investigate the level of localization required—using Irwin's method for Glinka's energy density assumption to hold. This includes evaluating a range of notch geometries, particularly blunt notches, where the radius (ρ) may determine the validity of the assumption. Although the analytical comparisons used here do not provide specific accuracy percentages, they do confirm that the SED method produces results within a reasonable range, establishing a solid foundation for further development.

5.3. Closing Remarks

In conclusion, this thesis has successfully developed and validated an analytical methodology that bridges the gap between elastic and inelastic stress-strain fields in high-strength steels. The results underline the potential for broader adoption of HSS in critical engineering applications, offering a pathway toward safer, more efficient, and cost-effective structural designs. While challenges remain, the insights gained from this research lay the foundation for future advancements in the field, benefiting both academic inquiry and practical implementation.

References

[1] R. Bjorhovde, “Development and use of high performance steel,” *Journal of Constructional Steel Research*, vol. 60, no. 3-5, pp. 393–400, 2004.

[2] B. EN, “En 1993-1-1, eurocode 3: Design of steel structures: Part 1-1: General rules and rules for buildings,” *European Committee for Standardization*, 2005.

[3] H.-P. Günther, J. Hildebrand, C. Rasche, *et al.*, “Welded Connections of High-Strength Steels For The Building Industry,” *Welding in the world*, vol. 56, no. 5-6, pp. 86–106, May 2012. DOI: 10.1007/bf03321353. [Online]. Available: https://doi.org/10.1007/bf03321353.

[4] N. Tavio, R. Anggraini, I. G. P. Raka, and N. Agustiar, “Tensile strength/yield strength (TS/YS) ratios of high-strength steel (HSS) reinforcing bars,” *AIP conference proceedings*, Jan. 2018. DOI: 10.1063/1.5038318. [Online]. Available: https://doi.org/10.1063/1.5038318.

[5] G. L. Louëdec, F. Pierron, M. A. Sutton, and A. P. Reynolds, “Identification of the Local Elasto-Plastic Behavior of FSW Welds Using the Virtual Fields Method,” *Experimental mechanics*, vol. 53, no. 5, pp. 849–859, Oct. 2012. DOI: 10.1007/s11340-012-9679-0. [Online]. Available: https://doi.org/10.1007/s11340-012-9679-0.

[6] C. Hou, “Fatigue analysis of welded joints with the aid of real three-dimensional weld toe geometry,” *International journal of fatigue*, vol. 29, no. 4, pp. 772–785, Apr. 2007. DOI: 10.1016/j.ijfatigue.2006.06.007. [Online]. Available: https://doi.org/10.1016/j.ijfatigue.2006.06.007.

[7] K. Molski and G. Glinka, “A method of elastic-plastic stress and strain calculation at a notch root,” *Materials science and engineering*, vol. 50, no. 1, pp. 93–100, Sep. 1981. DOI: 10.1016/0025-5416(81)90089-6. [Online]. Available: https://doi.org/10.1016/0025-5416(81)90089-6.

[8] T. Seeger and P. Heuler, “Generalized Application of Neuber’s Rule,” *Journal of testing and evaluation*, vol. 8, no. 4, pp. 199–204, Jul. 1980. DOI: 10.1520/jte11613j. [Online]. Available: https://doi.org/10.1520/jte11613j.

[9] P. Lazzarin, T. Lassen, and P. Livieri, “A notch stress intensity approach applied to fatigue life predictions of welded joints with different local toe geometry,” *Fatigue fracture of engineering materials structures*, vol. 26, no. 1, pp. 49–58, Dec. 2002. DOI: 10.1046/j.1460-2695.2003.00586.x. [Online]. Available: https://doi.org/10.1046/j.1460-2695.2003.00586.x.

[10] E. Z. Stowell, “Stress and strain concentration at a circular hole in an infinite plate,” Tech. Rep. Technical Note 2073, Apr. 1950. [Online]. Available: https://digital.library.unt.edu/ark:/67531/metadc55449/m2/1/high_res_d/19930082747.pdf.

[11] J. D. Besten and M. Kaminski, “Fatigue in Aluminium High-speed Craft: A large scale specimen design life parameter Estimate,” in *12th International Conference on Fast Sea Transportation*, Jan. 2013. [Online]. Available: https://repository.tudelft.nl/islandora/object/uuid%3A8ef2a6e5-e0c5-4519-aead-d21dcaf924e5.

[12] R. Mücke and O.-E. Bernhardi, “A constitutive model for anisotropic materials based on neuber’s rule,” *Computer methods in applied mechanics and engineering*, vol. 192, no. 37-38, pp. 4237–4255, 2003.

[13] P. Theocaris and E. Marketos, “Elastic-plastic analysis of perforated thin strips of a strain-hardening material,” *Journal of the mechanics and physics of solids/Journal of the Mechanics and Physics of Solids*, vol. 12, no. 6, pp. 377–380, Dec. 1964. DOI: 10.1016/0022-5096(64)90033-x. [Online]. Available: https://doi.org/10.1016/0022-5096(64)90033-x.

[14] G. Glinka, “Energy density approach to calculation of inelastic strain-stress near notches and cracks,” *Engineering fracture mechanics*, vol. 22, no. 3, pp. 485–508, Jan. 1985. DOI: 10.1016/0013-7944(85)90148-1. [Online]. Available: https://doi.org/10.1016/0013-7944(85)90148-1.

[15] R. W. Landgraf, F. D. Richards, and N. R. LaPointe, “Fatigue Life Predictions for a Notched Member Under Complex Load Histories,” *SAE technical papers on CD-ROM/SAE technical paper*

series, Feb. 1975. DOI: 10.4271/750040. [Online]. Available: https://doi.org/10.4271/750040.

[16] G. Kirsch, *Die Theorie der Elastizität und die Bedürfnisse der Festigkeitslehre*. Springer, 1898. [Online]. Available: https://books.google.nl/books?id=pvBuPwAACAAJ.

[17] S. P. Timoshenko and J. N. Goodier, *Theory of elasticity*. McGraw-Hill Book Company, Inc., Jan. 1934. [Online]. Available: http://cds.cern.ch/record/104369.

[18] G. E. Griffith, "Experimental investigation of the effects of plastic flow in a tension panel with a circular hole," Tech. Rep. Technical Note 1705, Sep. 1948. [Online]. Available: https://digital.library.unt.edu/ark:/67531/metadc54918/m2/1/high_res_d/19930082394.pdf.

[19] S. F. Obers, J. J. Overal, W. J. Wong, and C. L. Walters, "The effect of the yield to tensile strength ratio on stress/strain concentrations around holes in high-strength steels," *Marine structures*, vol. 84, p. 103 205, Jul. 2022. DOI: 10.1016/j.marstruc.2022.103205. [Online]. Available: https://doi.org/10.1016/j.marstruc.2022.103205.

[20] J. P. Dong and J. Hong, "Residual Stresses, Notch Stresses, and Stress Intensites at Welds - An Unified Assessment Procedure with Self-Consistency," *IASMiRT*, Jan. 2001. [Online]. Available: https://repository.lib.ncsu.edu/handle/1840.20/30634.

[21] P. Dong and F. W. Brust, "Welding Residual Stresses and Effects on Fracture in Pressure Vessel and Piping Components: A Millennium Review and Beyond," *Journal of pressure vessel technology*, vol. 122, no. 3, pp. 329–338, Apr. 2000. DOI: 10.1115/1.556189. [Online]. Available: https://doi.org/10.1115/1.556189.

[22] R. Bradford, "Through-thickness distributions of welding residual stresses in austenitic stainless steel cylindrical butt welds," *Proceedings of Residual Stresses-ICRS, 2000*, 2000.

[23] H. Y. Ban, G. Shi, Y. J. Shi, and Y. Q. Wang, "Research Progress on the Mechanical Property of High Strength Structural Steels," *Advanced materials research*, vol. 250-253, pp. 640–648, May 2011. DOI: 10.4028/www.scientific.net/amr.250-253.640. [Online]. Available: https://doi.org/10.4028/www.scientific.net/amr.250-253.640.

[24] *Building Code Requirements for Structural Concrete and Commentary*, 318-14. American Concrete Institute, Nov. 2014. DOI: 10.14359/51688187. [Online]. Available: https://doi.org/10.14359/51688187.

[25] N. AMakhutov and D. OReznikov, "Generalization of Neuber's Rule for the Assessment of Local Stresses and Strains in Stress Concentration Zones for a Wide Range of Applied Strains," *Procedia structural integrity*, vol. 14, pp. 199–206, Jan. 2019. DOI: 10.1016/j.prostr.2019.05.026. [Online]. Available: https://doi.org/10.1016/j.prostr.2019.05.026.

[26] W. J. Wong and C. Walters, "Effects of Strain Hardening and the Lode Dependence of the Fracture Strain Locus on Slant Fracture in Charpy V-Notch Impact Testing," vol. Volume 3: Materials Technology; Subsea Technology, ASME, Jun. 2024. DOI: 10.1115/omae2024-125635. [Online]. Available: https://doi.org/10.1115/omae2024-125635.

[27] A. Rezaei Mojdehi, "Application of meshless local petrov-galerkin (mlpg) method to three dimensional elasto-plastic problems based on deformation theory of plasticity," *Computer Modeling in Engineering and Sciences*, vol. 77, pp. 1–32, Jan. 2011. DOI: 10.3970/cmes.2011.077.001.

[28] Y. Qin, H. D. Besten, S. Palkar, and M. L. Kaminski, "Fatigue design of welded double sided T joints and double sided cruciform joints in steel marine structures: A total stress concept," *Fatigue Fracture of Engineering Materials Structures*, vol. 42, no. 12, pp. 2674–2693, Sep. 2019. DOI: 10.1111/ffe.13089. [Online]. Available: https://doi.org/10.1111/ffe.13089.

[29] J. H. Crews Jr, "Effects of loading sequence for notched specimens under high-low two-step fatigue loading," Tech. Rep., 1971.

[30] A. Conle and H. Nowack, "Verification of a neuber-based notch analysis by the companion-specimen method: The application of a notch analysis used in several computerized fatigue models is evaluated by comparison of predicted notch-root stress-strain behavior with direct measurements using the companion-specimen technique," *Experimental Mechanics*, vol. 17, pp. 57–63, 1977.

[31] J. Moon, B. Perrett, and P. Edwards, "A study of local stress histories in loaded and unloaded holes and their implications to fatigue life estimation," 1977.

[32] D. Mowbray and J. McConnelee, "Applications of finite element stress analysis and stress-strain properties in determining notch fatigue specimen deformation and life," *ASTM STP*, vol. 519, pp. 151–169, 1973.